On the breaking and broadening of internal solitary waves propagating in stratified fluid

by

John Grue, Atle Jensen, Per-Olav Rusås and Johan Kristian Sveen
Mechanics Division, Department of Mathematics,
University of Oslo, Norway

Solitary waves of depression propagating horizontally in a stratified fluid are investigated. The fluid has an upper shallow layer with linear stratification and a lower deep layer with constant density. The investigation is both experimental and theoretical. In the experiments, detailed recordings of the velocities induced by the waves are facilitated by recent developments of particle tracking velocimetry (PTV) and particle image velocimetry (PIV). Particular focus is paid to the role of wave breaking which is observed in the experiments. Incipient breaking is found to take place for moderately large waves in the form of generation of vortices in the leading part of the waves. The maximal fluid velocity close to the free surface, introduced by the waves, is then comparable to the linear long wave speed of the two-fluid system, and the wave amplitude is about half of the depth of the upper shallow layer. Wave amplitude is defined by the maximal negative excursion of the upper layer. The breaking increases in power with increasing wave amplitude and serves to limit the magnitude of the induced fluid velocity, the amplitude and the propagation speed. The breaking also introduces a broadening of the waves. A theoretical fully nonlinear two-layer model is developed in parallel with the experiments. In the theoretical model the fluid motion is assumed to be steady in a frame of reference moving with the wave. The Brunt-Väisälä frequency is constant in the upper layer and zero in the lower layer. Mathematical solution is obtained by means of integral equations. Results from the experiments, among others the vorticity induced by the waves, are compared with the theory. The effect of wave breaking is clearly seen in the experimental vorticity, particularly when compared with the theory, where in the latter wave breaking is not included. The theory does not predict the limiting amplitude, the limiting wave speed and the broadening of the waves. While the experiments are always run with a lower layer with depth h_1 being 4.13 times the depth h_2 of the upper, the results from the theoretical model show that the velocity field induced by the waves is similar for all depth ratios h_1/h_2 larger than about 3. This indicates that wave breaking and the effect of wave breaking is the same for all depth ratios h_1/h_2 larger than about 3.

1   Introduction

This study concerns solitary waves of depression propagating in a stratified fluid. The study has several motivations. One is a recent concern about the possible effect of internal waves on compliant offshore units for extraction of hydrocarbons in deep layered oceans. Such offshore units may be floating platforms or ships at the sea surface with connecting risers and cables to wells and equipment at the sea floor. The concern is the possible loads and induced vibrations of the risers and cables caused by internal waves. Another problem relates to a proposed submerged floating tunnel across Høgsfjorden in Rogaland in Norway. Internal waves may be generated and propagate in the layered fjord, and both the wave environment and the induced loads on such a tunnel are not yet sufficiently known. The dynamics of internal waves and their effects also represent other challenges. There are still several unsolved problems relating to the generation of internal waves, the

propagation properties and the break-up of internal waves entering a shore. Yet another aspect is that internal solitary waves may transport mass over long distances when the amplitude is sufficiently large. This is the case for the waves in the present study. Wave induced mass transport has implications among others to sediment transport in the ocean (geology) and to transport of larvae (biology). Some of the recent developments of the study of internal solitary waves and their effects may be found in Duda (1998).

We shall here be concerned with properties of solitary waves of depression propagating in a stratified fluid. The investigation may be relevant to the applications just mentioned, among others. The investigation combines experiments and theory. The experiments are performed in a wave tank with a two-layer fluid with a shallow upper layer of brine of linear stratification and a deep lower layer of brine of homogeneous density. The shape of the density profile is motivated by conditions in nature where solitary waves are observed, see figure 1. We generate solitary waves of mode one which propagate along the wave tank, see figure 2. The amplitude of the waves, defined by the maximal negative excursion of the upper layer, is in a rather large range. Particle tracking velocimetry (PTV) and particle image velocimetry (PIV) is applied to make detailed recordings of the induced velocities due to the waves.

Surprisingly, we shall find that wave breaking occurs for rather moderate amplitude. The breaking takes place by formation of small vortices in the leading part of the waves (for illustration, see e.g. figure 13). Further, we shall find that the breaking serves to limit the amplitude, the propagation speed and the magnitude of the induced fluid velocity. Also, broadening of the waves takes place when the volume of the wave exceeds a certain value. We shall in the paper pay much attention to the wave breaking and the effect of wave breaking.

With the purpose of providing a thorough understanding of the experiments and to interpret the results, we develop a theoretical model of the experiments. We consider steady wave solutions in a two-layer fluid, where the Brunt-Väisälä frequency is constant in the upper layer and zero in the lower layer. (The theoretical model does not include transient effects like wave breaking.) The equations of the fully nonlinear model are derived along the lines of previous studies (Long, 1958; Yih, 1960; Tung, Chan & Kubota, 1982; Turkington, Eydeland & Wang, 1991). We have found it advantageous to solve the the mathematical problem by means of integral equations. This solution procedure is well suited to the present two-layer model, where the Brunt-Väisälä frequency is discontinuous at the transition between the upper and lower layer. We compare several quantities from the experiments with the theory, among others the vorticity induced by the waves. The effect of wave breaking is clearly seen in the experimental vorticity, particularly when compared with the theory where wave breaking is not included.

In a recent study, Derzho & Grimshaw (1997) develop a long wave model of solitary waves with a vortex core propagating in a shallow layer of stratified fluid. They give numerical results for a linear stratification of the total fluid layer, finding that the vortex core in their model introduces a broadening of the waves. Furthermore, they find that the propagation speed increases somewhat less than linearly with the wave amplitude, close to a saturation. The results by Derzho & Grimshaw are in principle somewhat related to ours. Their numerical values of the broadening effect and the nonlinear wave speed are small, however, and may be difficult to observe in experiments like e.g. those we describe here. Furthermore, their vortex core, with constant vorticity, is rather different from what we observe in the experiments for the large waves. These waves, in the experiments, have an upper region containing pronounced vorticity with rather strong oscillations about a nonzero mean. The velocity field in our experiments for the large waves is clearly three-dimensional.

We further note a rather fundamental difference between our study and that of Derzho
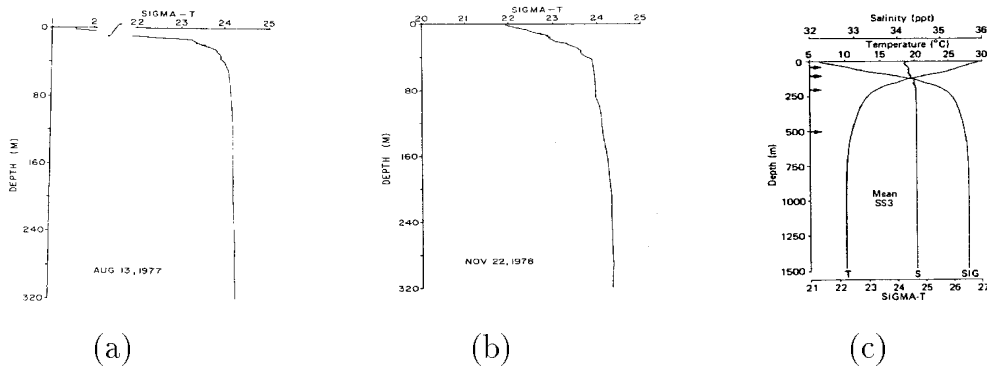
Figure 1: Examples of density profiles in large scale where internal solitary waves are observed. (a) and (b) at the Knight Inlet (Farmer and Smith, 1980, figure 2), (c) in the Sulu Sea (Apel et al. 1985, figure 3).

and Grimshaw. In our, we consider waves in a two-layer model which provides a wave guide. We study how the breaking determines the wave properties when the amplitude is large. The model of Derzho and Grimshaw has, on the other hand, no wave guide when they apply a linear stratification and the vortex core is absent. A direct experimental verification of the theoretical examples given by Derzho and Grimshaw would be interesting.

We note that vortex cores in internal solitary waves of mode 2 have been previously described in experimental works by Davis & Acrivos (1967), Maxworthy (1980), Stamp & Jacka (1995), however without giving detailed results for the velocity fields, the breaking and the broadening of the waves. Further, we note that the theoretical fully nonlinear models predict internal waves containing a region of recirculating fluid when the amplitude increases beyond a certain value. The (theoretical) fluid velocity at the free surface above the centre of the wave becomes equal to the propagation speed when the recirculating region appears (critical speed), indicating that breaking should occur for realistic waves. We find that breaking of the waves appear rather different in the experiments from what can be anticipated by theory. Further, incipient breaking occurs for waves with considerably smaller amplitude than indicated by theory.

The paper is organized as follows: §2 describes the experimental arrangements and the PTV and PIV techniques. §3 describes the theoretical two-layer model, the integral equation method and the numerical procedure. In §4 results for the propagation speed of the waves are given. Results for waves with small amplitude are given in §5. Detailed results of incipent breaking, in terms of velocity and vorticity plots, are given in §6. The wave amplitude is then moderate. In §7 results for waves with limiting amplitude and propagation speed, and broadening of the waves are given. Finally, §8 contains concluding remarks.

2 Experiments

2.1 Calibration of the two-layer model

The experiments are carried out in a wave tank in the Hydrodynamical Laboratory at the University of Oslo. The wave tank is totally 25m long and 0.5m wide. We have found it convenient to perform experiments in sections of the wave tank being either 12.3m or 18.4m long. To calibrate the two-layer fluid we first prepare a lower homogeneous layer of brine with density $\rho_0 = 1.022...\text{gcm}^{-3}$ and depth h_1. A layer of fluid with depth h_2
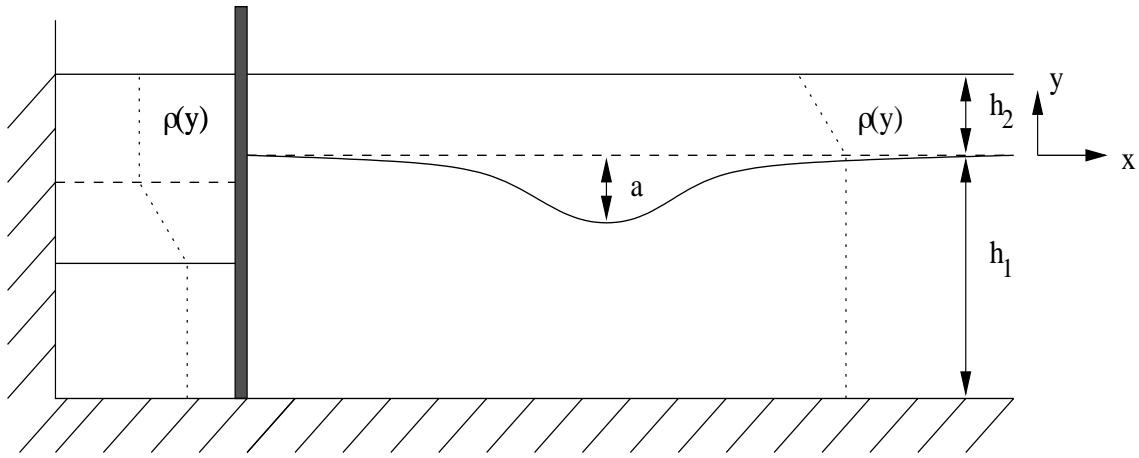
Figure 2: Sketch of the experiment.

and linear stratification is then very gently filled on top of the lower layer. The density of the upper layer varies from $\rho_0 = 1.022...\mathrm{gcm}^{-3}$ at the bottom of the layer to ρ_1 at the top. ρ_1 is in the interval $0.999...\mathrm{gcm}^{-3}$ to $1.004...\mathrm{gcm}^{-3}$. We use fleets with sponges to calibrate the upper layer. The time period of the filling can be several hours. The density profiles are recorded by a Yokogawa SC12 meter, which determines the density from the local conductivity of the fluid. Complementary density measurements are obtained by a Mettler-Toledo DA-300M density meter which determines the density from the weight of the water with an accuracy of five significant digits. The values of ρ_0 and ρ_1 may vary somewhat from run to run due to practical reasons. Such a variation is, however, unimportant to the results when the linear long wave speed, c_0, is used as reference speed. The latter is in all cases determined theoretically by equation (18).

To generate waves we gently add a volume of fresh water (of density $0.999...\mathrm{gcm}^{-3}$) behind a gate which is lowered at one end of the tank. A corresponding mass of the lower fluid then slowly moves to the other side of the gate such that hydrostatic balancy is maintained. The depths of the layers in the main part of the tank are in each experiment $h_1 = 62\mathrm{cm}$ and $h_2 = 15\mathrm{cm}$, while the initial volume of fresh water behind the gate is varied. By removing the gate a solitary depression wave is generated, propagating along the wave tank. A sketch of the experiment is given in figure 2.

2.2   Particle tracking and particle image velocimetry

Particle tracking velocimetry (PTV) and particle image velocimetry (PIV) represent powerful experimental techniques to quantify the velocities and the underlying dynamics of the waves observed in the wave tank. We shall here use both methods. In the PTV method individual particles are traced in sequences of images. This method is ideal when the local fluid accelerations are relatively small, which is the case in the present experiments when the wave amplitude is small or moderate. In the PIV method the spatial cross-correlation between the position of groups of particles at two subsequent time-instants is evaluated to estimate the local fluid velocity. We analyze the motion due to the moderate waves using both PTV and PIV. For the larger waves, indroducing rather rapid fluid motion and strong variations of the vorticity, we find that PIV is required for precise measurements of the fluid motion.

Recordings are made in vertical sections of the wave tank by three monochrome COHU

4

4912 CCD cameras with a resolution of 575×560 pixels. The cameras are placed at positions 6.95m, 10.63m and 15.31m from the wall at the upper end of the tank where the wave begins. A light sheet with thickness 5cm and distance of 10cm from the glass wall of the tank is created in each section. The light sheets are vertical and parallel to the side of the tank. Powerful overhead projectors are used as light sources. The illuminated sections are seeded with particles of pliolite VTAC with diameter in the range of 0.8–1mm. The particles are treated in wetting agent for some time to obtain an effective neutral bouyancy for the range of the density profile.

The recording section seen by each camera is 50cm long and 40cm high. This means that a particle at rest normally is covered by four pixels in the CCD-chip in the camera. Each cell in the CCD-chip is charged for 1/50s. The transmission of the even and odd lines of the CCD-chip is sequential, however, giving an effective exposure time of 3/100s. In the experiments with small to moderate wave amplitude we observe a maximal velocity up to about 10cms^{-1}, giving as result exposures of the pliolite particles covering up to about eight pixels. For the largest waves, velocities up to about 20cms^{-1} are introduced in the fluid. In these runs we use a mechanical shutter in front of the cameras with the purpose to enhance the accuracy. The effective exposure time then becomes 1/100s. The time between each frame is 1/25s.

The video recordings are digitized by a frame grabber card for subsequent analysis. Typically we identify a number of 1200-4000 particles in each frame. For the PTV we trace particles during five frames using the DigImage program developed and described by Dalziel (1992). In an earlier work, Grue et al. (1999), we used this method to analyze the velocities induced by internal solitary waves in a two-layer fluid with homogeneous density in each of the layers. The measurements were compared with theoretical computations. We found in that investigation that the error in the measured velocities, relative to the linear long wave speed, was less than about 7-8% in all cases. That investigation includes further details details of the PTV method used here.

For PIV analysis we have implemented the method outlined by Willert and Gharib (1991). In addition, we employ interrogation window shifting as proposed by Westerweel, Dabiri and Gharib (1997). The images are interrogated in three steps where the two first steps are used to estimate the window shift with integer accuracy. In the final step the displacement is estimated to sub pixel accuracy using a three point gaussian peak fit. Images are interrogated using interrogation windows 32×32 pixels. In a few experiments we have also used 64×64 pixels due to insufficient particle seeding. The final velocity vectors are validated using a signal to noise ratio filter, where the signal to noise ratio is determined by the highest peak in the correlation plane divided by the second highest peak. For intermediate waves we normally require that this ratio is larger than 1.3, while for the large waves we use a value of 1.05. This less stringent value has to be applied mainly due to the turbulent character of a kernel of the large waves, with an accompanying increase of noise and decrease of peak height in the correlation plane. Vectors not satisfying this threshold are rejected and replaced by the mean of the surrounding vectors. Finally we apply a global histogram operator that effectively removes vectors that are significantly different from their neighbours. By using a relatively large threshold value for this filter we are usually able to remove most of the spurious vectors present in the field. The PIV-algoritm may be found in Sveen (1998).

3 Theory

3.1 Two-layer model

As noted in the Introduction, we develop a theoretical model in parallel with the experiments. The equations of the fully nonlinear model are derived along the lines of previous studies (Long, 1958; Yih, 1960; Tung et al. 1982; Turkington et al. 1991). Coordinates $O - xy$ are introduced, with the x-axis horizontal and the y-axis vertical, and with unit vectors $\mathbf{i}$ and $\mathbf{j}$ accordingly. We consider motion in two dimensions where waves of permanent form is propagating with speed c horizontally in the fluid. Viewing the problem in a frame of reference which follows the waves, the motion becomes steady, with a horizontal current with speed c along the negative x-axis in the far-field. The undisturbed fluid has a vertical density profile $\rho(y)$. We assume that the fluid is incompressible and inviscid. The former means that $\nabla \cdot \mathbf{v} = 0$ where $\mathbf{v} = (u, v)$ denotes the fluid velocity. Conservation of mass, $\nabla \cdot (\rho \mathbf{v}) = 0$, then gives that $\mathbf{v} \cdot \nabla \rho = 0$. Following the procedure of Yih (1960) we introduce pseudo velocities by $u' = (\rho/\rho_0)^{1/2}u$, $v' = (\rho/\rho_0)^{1/2}v$, where ρ_0 is a reference density. Furthermore we introduce a pseudo stream function Ψ' such that $\mathbf{v}' = \nabla \Psi' \times \mathbf{k}$ where $\mathbf{k} = \mathbf{i} \times \mathbf{j}$. It follows that $\rho = \rho(\Psi')$. From the equations of motion the following relation may be derived (Yih, 1960)

$$\rho_0 \nabla^2 \Psi' + gy \frac{d\rho}{d\Psi'} = \frac{dH(\Psi')}{d\Psi'} = h(\Psi'), \tag{1}$$

where $\nabla^2 \Psi'$ determines the pseudo vorticity and $H = p + \frac{1}{2}\rho(u^2 + v^2) + \rho gy$ is the Bernoulli constant being conserved along a streamline determined by $\Psi' = \text{constant}$. Furthermore, p denotes pressure and g the acceleration due to gravity. $dH/d\Psi'$ is determined in the far-field, giving

$$\frac{dH}{d\Psi'} = \left(\frac{dp}{dy} + \rho g\right)\frac{dy}{d\Psi'} + \frac{c^2}{2}\frac{d\rho}{d\Psi'} + gy\frac{d\rho}{d\Psi'}. \tag{2}$$

The vertical component of the equation of motion becomes in the far-field $p_y + \rho g = 0$, which means that the first term on the right of (2) is zero. The pseudo stream function is then decomposed by $\Psi' = \Psi'_\infty + \psi'$, where Ψ'_∞ satisfies

$$\frac{d\Psi'_\infty}{dy} = -c\left(\frac{\rho}{\rho_0}\right)^{1/2} \tag{3}$$

giving

$$\nabla^2 \Psi'_\infty = \frac{c^2}{2\rho_0}\frac{d\rho}{d\Psi'}. \tag{4}$$

Since $d\rho/d\Psi'$ is constant along each streamline, (1) becomes

$$\rho_0 \nabla^2 \psi' + g(y - y_\infty)\frac{d\rho}{d\Psi'} = 0 \tag{5}$$

where y and y_∞ are vertical coordinates on the same streamline, with y_∞ in the far-field.

From now on we apply the Boussinesq approximation, i.e. exploit that $\Delta\rho/\rho$ is small. Integrating (3) we find $\Psi'_\infty = -cy[1 + O(\Delta\rho/\rho)]$, giving

$$y - y_\infty = \psi'/c. \tag{6}$$

Furthermore we have

$$\frac{g}{\rho_0}\frac{d\rho}{d\Psi'} = \frac{g}{\rho_0}\frac{d\rho}{dy}\frac{dy}{d\Psi'} \simeq \frac{N^2}{c}[1 + O(\Delta\rho/\rho)], \tag{7}$$

6

where $N^2 = -(g/\rho_0)(d\rho/dy)$ determines the Brunt-Väisälä frequency. Within the Boussinesq approximation we may also replace the pseudo stream function by the stream function Ψ such that $\mathbf{v} = \nabla\Psi \times \mathbf{k}$. Correspondingly, Ψ'_∞ and ψ' are replaced by Ψ_∞ and ψ, respectively. The motion is thus governed by the Helmholtz equation, i.e. $\nabla^2\psi + (N^2/c^2)\psi = 0$.

Relevant to the experiments we consider a two-layer model where the undisturbed fluid has an upper layer with linear density profile and a lower layer with constant density, i.e.

$$\rho(y) = \begin{cases} \rho_0 - \Delta\rho\, y\,/h_2, & \text{for} & 0 < y < h_2, \\ \rho_0, & \text{for} & -h_1 < y < 0, \end{cases} \tag{8}$$

such that the line $y = 0$ separates the two layers. The upper layer extends in the interval $0 < y < h_2$ and the lower layer in the interval $-h_1 < y < 0$. The Brunt-Väisälä frequency becomes a constant in the upper layer, and is there determined by $N_0^2 = (\Delta\rho\, g)/(\rho_0 h_2)$. In the lower layer the Brunt-Väisälä frequency becomes zero. Let $\psi = \psi_2$ in the upper layer and $\psi = \psi_1$ in the lower. Then ψ_2 satisfies the Helmholtz equation in the upper layer, i.e.

$$\nabla^2\psi_2 + \frac{N_0^2}{c^2}\psi_2 = 0\,. \tag{9}$$

ψ_1 satisfies the Laplace equation in the lower layer, i.e.

$$\nabla^2\psi_1 = 0\,. \tag{10}$$

The upper boundary of the upper layer is a free surface. With $\Delta\rho/\rho$ small this boundary may be approximated by a horizontal rigid lid. We assume that the bottom of the lower layer is horizontal at $y = -h_1$. Thus,

$$\psi_2 = 0 \quad \text{at} \quad y = h_2, \tag{11}$$

$$\psi_1 = 0 \quad \text{at} \quad y = -h_1. \tag{12}$$

The two layers are separated by the streamline with vertical coordinate η where $\eta \to 0$ for $x \to \pm\infty$. The kinematic boundary condition between the layers gives that

$$\frac{\partial\psi_2}{\partial s} - c\frac{\partial\eta}{\partial s} = 0 \quad \text{at} \quad y = \eta, \tag{13}$$

$$\frac{\partial\psi_1}{\partial s} - c\frac{\partial\eta}{\partial s} = 0 \quad \text{at} \quad y = \eta, \tag{14}$$

$$\frac{\partial\psi_1}{\partial n} = \frac{\partial\psi_2}{\partial n} \quad \text{at} \quad y = \eta, \tag{15}$$

where s denotes the arc length of the streamline $y = \eta$ and n the normal, pointing out of the lower fluid layer.

3.2   The wave speed for long linear waves

Linear waves with wavenumber ν and wave speed c_0 may propagate horizontally in the fluid. The stream function ψ_2 in the upper layer then satisfies (9), with c replaced by c_0, while ψ_1 satisfies (10). Looking for solutions on the form $\psi_{1,2}(x,y) = \hat{\psi}_{1,2}(y)\cos\nu x$ satisfying (11)–(12) and (13)–(14), the latter two at $y = 0$, we find in the long wave limit

$$\psi_2 = ac_0\frac{\sin(N_0(y - h_2)/c_0)}{\sin(N_0 h_2/c_0)}\cos\nu x\,, \tag{16}$$

$$\psi_1 = -ac_0(1 + y/h_1)\cos\nu x\,. \tag{17}$$

The wave velocity is determined using (15), i.e. putting $\partial\psi_1/\partial y = \partial\psi_2/\partial y$ at $y = 0$. This gives

$$\frac{N_0 h_2}{c_0} \cot \frac{N_0 h_2}{c_0} + \frac{h_2}{h_1} = 0, \tag{18}$$

where c_0 is obtained for $N_0 h_2/c_0$ in the interval $(\pi/2, \pi)$. For $h_2/h_1 \to 0$ the speed becomes $c_0 = N_0 h_2/(\pi/2)$. In our experiments, with $h_2/h_1 = 15/62$, the linear long wave speed is $c_0 = N_0 h_2/1.711...$

3.3   Solution by integral equations

We solve the nonlinear problem (9)–(15) by means of integral equations and introduce two Green functions G_1 and G_2. The first Green function is a source at $(x, y) = (x', y')$ and satisfies the Laplace equation (10), i.e.

$$G_1(x, y, x', y') = \ln \frac{r}{r_1}. \tag{19}$$

The second Green function is a source at $(x, y) = (x', y')$ and satisfies the Helmholtz equation (9), i.e.

$$G_2(x, y, x', y') = \frac{\pi}{2}\left[Y_0(Kr) - Y_0(Kr_2)\right], \tag{20}$$

where Y_0 denotes the Bessel function of second kind of order zero and $K = N_0/c$. Furthermore,

$$r = [(x - x')^2 + (y - y')^2]^{1/2}, \tag{21}$$
$$r_1 = [(x - x')^2 + (y + y' + 2h_1)^2]^{1/2}, \tag{22}$$
$$r_2 = [(x - x')^2 + (y + y' - 2h_2)^2]^{1/2}. \tag{23}$$

We let the stream functions be determined by source distributions, i.e.

$$\psi_1 = \int_I \sigma_1(s') G_1(x, y, x'(s'), y'(s')) ds', \tag{24}$$

$$\psi_2 = \int_I \sigma_2(s') G_2(x, y, x'(s'), y'(s')) ds', \tag{25}$$

where $\sigma_1(s)$ and $\sigma_2(s)$ denote source strengths, I denotes the contour $y = \eta$ and s arclength. We then consider the tangential and normal derivatives of ψ_1 and ψ_2 at I, finding

$$\frac{\partial\psi_{1,2}}{\partial s} = PV \int_I \sigma_{1,2}(s')\frac{\partial G_{1,2}}{\partial s} ds' \tag{26}$$

$$\frac{\partial\psi_1}{\partial n} = -\pi\sigma_1(s) + \int_I \sigma_1(s')\frac{\partial G_1}{\partial n} ds', \tag{27}$$

$$\frac{\partial\psi_2}{\partial n} = \pi\sigma_2(s) + \int_I \sigma_2(s')\frac{\partial G_2}{\partial n} ds', \tag{28}$$

where in (26) PV denotes principal value. The boundary conditions (13)–(15) then gives

$$PV \int_I \sigma_1(s')\frac{\partial G_1}{\partial s} ds' - c\frac{\partial\eta}{\partial s} = 0, \tag{29}$$

$$PV \int_I \sigma_2(s')\frac{\partial G_2}{\partial s} ds' - c\frac{\partial\eta}{\partial s} = 0, \tag{30}$$

$$-\pi[\sigma_1(s) + \pi\sigma_2(s)] + \int_I \left(\sigma_1(s')\frac{\partial G_1}{\partial n} - \sigma_2(s')\frac{\partial G_2}{\partial n}\right) ds' = 0. \tag{31}$$

Choosing h_2 as length scale and c_0 as velocity scale (and h_2/c_0 as time scale) we determine $N_0 h_2/c_0$ by (18). Then the nondimensional quantities Kh_2, σ_1/c_0, σ_2/c_0, η/h_2 and c/c_0 depend on the parameters h_1/h_2 and η_{max}/h_2, and not on $\Delta\rho/\rho$. Thus, within the Boussinesq approximation, the actual value of $\Delta\rho/\rho$ enters only in the problem through c_0.

3.4 Numerical procedure

We look for symmetric solutions with respect to $x = 0$ which means that $\psi_{1,2}$ may be expressed by

$$\psi_{1,2} = \int_0^\infty \sigma_{1,2}(s')[G_{1,2}(x,y,x'(s'),y'(s')) + G_{1,2}(x,y,-x'(s'),y'(s'))]ds'. \qquad (32)$$

To discretize the equations we introduce a ξ-variable as coordinate along I replacing the arc length s as integration parameter. The collocation points $\xi = 1,2,3,...,N$ are equally distributed in s which means that $s_\xi = \Delta s$ where $s_\xi \equiv ds/d\xi$. Equation (32) then becomes

$$\psi_{1,2} = \int_1^N \sigma_{1,2}(s')[G_{1,2}(x,y,x'(\xi'),y'(\xi')) + G_{1,2}(x,y,-x'(s'),y'(s'))]\Delta s\,d\xi'. \qquad (33)$$

It is convenient to introduce the complex variable $z = x + iy$ and the complex functions $g_1(z,z')$ and $g_2(z,z')$ by

$$g_1(z,z') = \Delta s\left(\frac{\partial}{\partial s} - i\frac{\partial}{\partial n}\right) G_1(x,y,x',y') = \frac{z_\xi}{z-z'} - \frac{z_\xi}{z-z'^* + 2ih_1} \qquad (34)$$

$$g_2(z,z') = \Delta s\left(\frac{\partial}{\partial s} - i\frac{\partial}{\partial n}\right) G_2(x,y,x',y')$$
$$= \frac{\pi}{2}\left(-KrY_1(Kr)\frac{z_\xi}{z-z'} + Kr_2Y_1(Kr_2)\frac{z_\xi}{z-z'^* - 2ih_2}\right). \qquad (35)$$

The integrals in (29)–(31) and (33) are evaluated by using the trapezoid rule, except in the vicinity of the poles, where we adopt the procedure described by Dold and Peregrine (1986). Expanding the integrands (in vicinity of the poles) in powers of $(\xi - \xi')$ we arrive at the following discretized equations

$$\sum_{\xi=1}^N \mathcal{A}_k(\xi,\xi')\sigma_k(\xi') - \sigma_{k,\xi}(\xi) = c\eta_{,\xi}(\xi)/\Delta s, \quad k = 1,2, \qquad (36)$$

$$-\pi(\sigma_1 + \sigma_2) + \sum_{\xi=1}^N [\mathcal{B}_1(\xi,\xi')\sigma_1(\xi') - \mathcal{B}_2(\xi,\xi')\sigma_2(\xi')] = 0, \qquad (37)$$

where the matrices $\mathcal{A}_k(\xi,\xi')$ and $\mathcal{B}_k(\xi,\xi')$ read

$$\mathcal{A}_1(\xi,\xi') - i\mathcal{B}_1(\xi,\xi') = \begin{cases} g_1(z,z') + g_1(z,-z'^*), & \xi' > 1,\ \xi' \neq \xi \\ g_1(z,z'), & \xi' = 1,\ \xi' \neq \xi \\ \frac{z_{\xi\xi}}{2z_\xi} - \frac{z_\xi}{z-z'^*+2ih_1} + g_1(z,-z^*), & \xi' > 1,\ \xi' = \xi \\ \frac{z_{\xi\xi}}{2z_\xi} - \frac{z_\xi}{z-z'^*+2ih_1} & \xi' = \xi = 1 \end{cases} \qquad (38)$$

$$\mathcal{A}_2(\xi,\xi') - i\mathcal{B}_2(\xi,\xi') = \begin{cases} g_2(z,z') + g_2(z,-z'^*), & \xi' > 1,\ \xi' \neq \xi \\ g_2(z,z'), & \xi' = 1,\ \xi' \neq \xi \\ \frac{z_{\xi\xi}}{2z_\xi} + \frac{\pi}{2}Kr_2Y_1(Kr_2)\frac{z_\xi}{z-z'^*-2ih_2} + g_2(z,-z^*), & \xi' > 1,\ \xi' = \xi \\ \frac{z_{\xi\xi}}{2z_\xi} + \frac{\pi}{2}Kr_2Y_1(Kr_2)\frac{z_\xi}{z-z'^*-2ih_2} & \xi' = \xi = 1 \end{cases}$$
$$(39)$$

and an asterix denotes complex conjungate.

The equations are solved by considering c/c_0, $\eta(1)/h_2$, $\sigma_1(1)/c_0$, $\sigma_2(1)/c_0$, $x(\xi)_\xi/h_2$, $\eta(\xi)_\xi/h_2$, $\sigma_1(\xi)_\xi/c_0$ and $\sigma_2(\xi)_\xi/c_0$ for $\xi = 2,...,N$, as unknowns. Furthermore, we require that $\eta(N) = 0$ and that the source strength is smooth at the truncation of I, i.e. $\sigma_{1,\xi}(N-$

$1) = \sigma_{1,\xi}(N)$ and $\sigma_{2,\xi}(N-1) = \sigma_{2,\xi}(N)$. The system is solved by applying a variant of the Newton-Rapson method for a prescibed amplitude a/h_2, i.e. $\eta(1)/h_2 = -a/h_2$. At each iterative step, $x(\xi)/h_2$, $\eta(\xi)/h_2$, $\sigma_1(\xi)/c_0$ and $\sigma_2(\xi)/c_0$ are obtained from their respective derivatives by the 4 point Lagrangian integration formula, i.e.

$$\int_{\xi-1}^{\xi} f(\zeta)\mathrm{d}\zeta = \frac{1}{24}\left[-f(\xi+1) + 13f(\xi) + 13f(\xi-1) - f(\xi-2)\right].\qquad(40)$$

The second derivative $z_{\xi\xi}$ is found by using the 4 point Lagrangian difference formula.

The differentiations for obtaining the Jacobi matrix in the secant method are approximated using first order discrete differences, with the matrices A_k and B_k considered as constants during the differentiations. This procedure increases the number of iterations somewhat as compared to using the full Jacobi matrix, but leads to a relatively faster scheme.

4   The propagation speed of solitary waves

Internal depression waves are generated in the wave tank as described in §2.1. Immediately after the gate is opened, the fluid motion is locally rather violent at the position of the gate. After a while, however, the initial disturbance develops into a solitary depression wave propagating along the tank, and the initially violent motion disappears. The wave has quite distinct properties, among others a clearly defined propagation speed, which is the first quantity we measure. To do so, we measure the (horizontal) speed of a vertical line through the centre of the wave, or almost the centre of the wave, which is characterized by a vanishing vertical fluid velocity. This line corresponds to the symmetry line in the theoretical model (see eq. (32) with $x = 0$). More specifically we proceed as follows:

1. The experimental velocity matrix is obtained in the coordinates (x_m, y_n), $m = 1, ..., M$, $n = 1, ..., N$. In a frame capturing the centre of the wave, we search in the velocity matrix for the intervals $(x_{\tilde{m}}, x_{\tilde{m}+1})_n$, $\tilde{m} = 1, ..., \tilde{M}$, $(1 \leq \tilde{M})$, $n = 1, ..., N$, where the vertical component of the velocity changes sign.

2. The position of the vertical line is determined by the median of the endpoints of the intervals, with smallest vertical velocity.

The propagation speed c is estimated by the travel distance of this line between two cameras divided by the elapsed time. The method is carefully checked and is found to be robust.

The waves in the experiments have no clearly defined amplitude. For example, we are from the measured fluid velocities unable to identify a sharp boundary between the upper stratified layer and the lower homogeneous layer. (Measurements of the actual density profile would perhaps resolve this problem.) The theoretical model may be applied to define an amplitude of the wave, on the other hand, since the boundary between the two layers there is sharp. We therefore define the amplitude of the experimental wave from the theoretical model by fitting the experimental and theoretical velocity fields. For the largest waves the experiments exhibit a region with strong mixing close to the free surface above the centre of the wave. In such cases we compare the experimental and theoretical velocity fields below the region with mixing. This way of estimating the experimental wave amplitude is about as accurate as the PTV and PIV techniques.

In figure 3 is shown the measured and theoretical speed of the solitary waves as function of the wave amplitude. Generally, the agreement between experiment and theory is good for all wave amplitudes. There is particularly good agreement between the experiment

and the theory for small wave amplitude. This is true not only for the propagation speed, but also for the entire velocity field induced by the wave. (Results for the latter are given in §5.) This good agreement between the measured and computed c, for small a/h_2, illustrates the usefulness of the method of extracting c in the experiments, among others.

The measurements of the propagation speed exhibit some scatter for wave amplitudes in the range $a/h_2 \sim 0.5 - 0.8$. Furthermore, it is rather evident that the experimental c exceeds the theoretical one in this amplitude range. We observe in these experiments that localized regions with strong variations of the vorticity develop in the fore part of the wave and above the center of the wave. The presence of these regions represent a qualitative difference between the experiments and the theory, since they are not present in the latter.

By generating waves increasing the initial volume, we encounter a maximal speed and a maximal amplitude of the waves. The maximal observed propagation speed is about 1.8 times the linear long wave speed, and the maximal amplitude is about 1.25 times the depth of the upper shallow layer. We note that the results exhibit a good correspondence between the measured and computed propagation speed even for the large waves. This is rather surprising, since the theory does not capture several effects observed in the experiments, when the wave amplitude is large. The most visible difference is the rather dominant region with strong mixing which takes place above the centre of the wave in the experiments. Furthermore the theory does not predict the maximal values of the amplitude, the propagation speed and the fluid velocities observed in the experiments. The theory predicts instead a continuous growth of the amplitude and wave speed beyond the experimental maximal values. The theory also predicts a region of recirculating fluid above the centre of the wave when the theoretical amplitude exceeds $a/h_2 = 0.855$. In this region the fluid velocity at the free surface becomes larger than the propagation speed, indicating that breaking should occur for realistic waves. This is true, as the experiments show. The wave breaking in the experiments occurs rather different than what can be anticipated by theory, however, with incipient breaking for wave amplitude as small as a/h_2 about 0.5 (see §6).

The results in figure 3 show that the propagation speed is a linear function of the amplitude, practically speaking. This means that weakly nonlinear theory, which is valid for small a/h_2, should predict a propagation speed that fit with the measurements and the nonlinear theory even for amplitudes which are not small.

5 Properties for waves with small amplitude

The velocity field induced by the waves is then examined. First we study waves with small (finite) amplitude. We find good agreement between experiment and theory (figures 4–8). This good agreement shows that the theory provides a useful description of the solitary waves under consideration, for small (finite) amplitude. Moreover, this agreement documents the usefulness of the way of generating the waves in the wave tank, with the purpose to investigate the properties of solitary waves in a fluid with a continuous stratification.

The results exhibit that the fluid velocities close to the free surface, induced by the waves, become comparable with the linear long wave speed even for rather moderate wave amplitude. More specifically, the maximal horizontal velocity is about 65% of c_0 for $a/h_2 = 0.4$ (figure 6).

The smallest waves exhibit a decay in the amplitude during the propagation along the tank, as visualized in figures 4–5. Such a decay is, however, less pronounced for the larger waves, to be discussed in §§6–7.
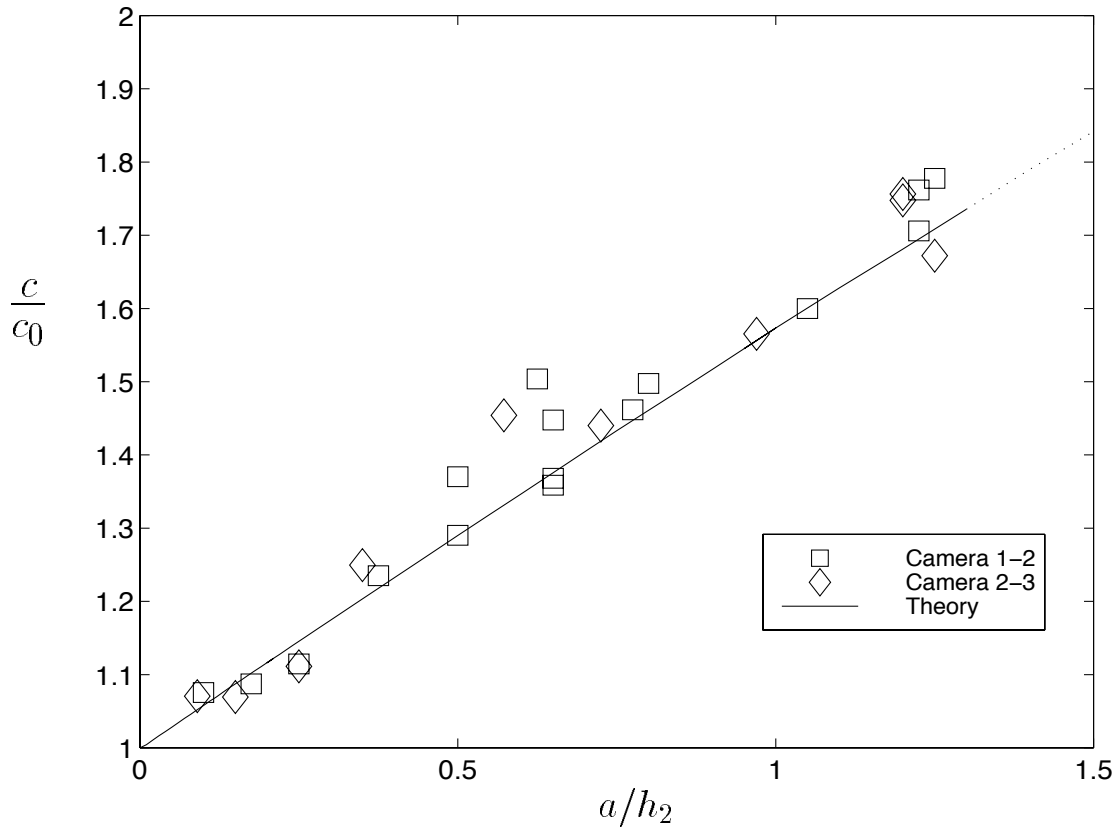
Figure 3: Propagation speed c vs. wave amplitude a. c_0 determined theoretically by (18). Cameras at positions 6.95m, 10.63m and 15.31m from the wall at the upper end of the tank. (Layer thicknesses are $h_2 = 15$ cm (upper) and $h_1 = 62$ cm (lower). Linear stratification in the upper layer. Homogeneous density in the lower layer.)
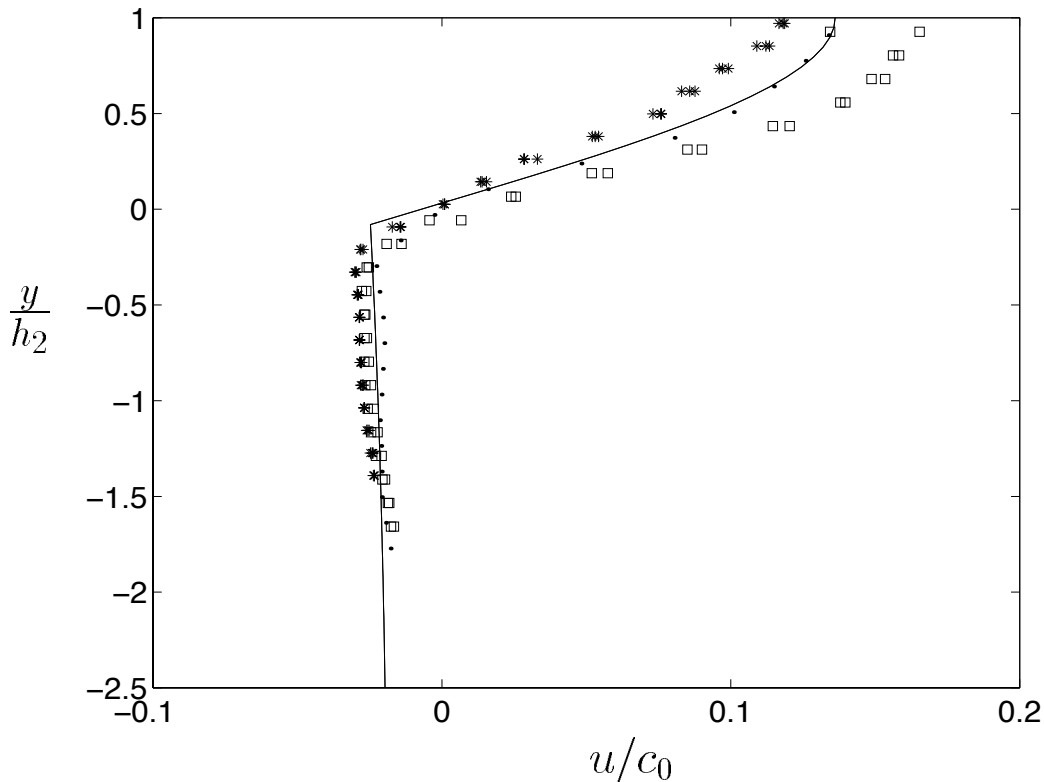
Figure 4: Velocity profile at the maximal depression of the wave. PTV: squares (camera 1), dots (camera 2), stars (camera 3). Initial volume: 10 dm^3. Theory with $a/h_2 = 0.1$ (solid line).

With the purpose of a closer comparison between the experimental and theoretical results, we evaluate the vorticity, $\omega = \partial u/\partial y - \partial v/\partial x$, from the PTV analysis using a standard difference method, and from the theory by (5). The vorticity at a position of the tank is initially zero, and reduces to zero when the wave has disappeared. The vorticity during the passage of the wave is illustrated in figures 7 and 8. We observe again the good correspondence between experiment and theory at the first camera position (figure 7). At the second camera we note that a somewhat different behaviour of the vorticity takes place in the experiments than in the theoretical model. This difference is visible only in the leading part of the wave rather close to the free surface, as illustrated in figure 8. This difference becomes more pronounced for the larger waves.
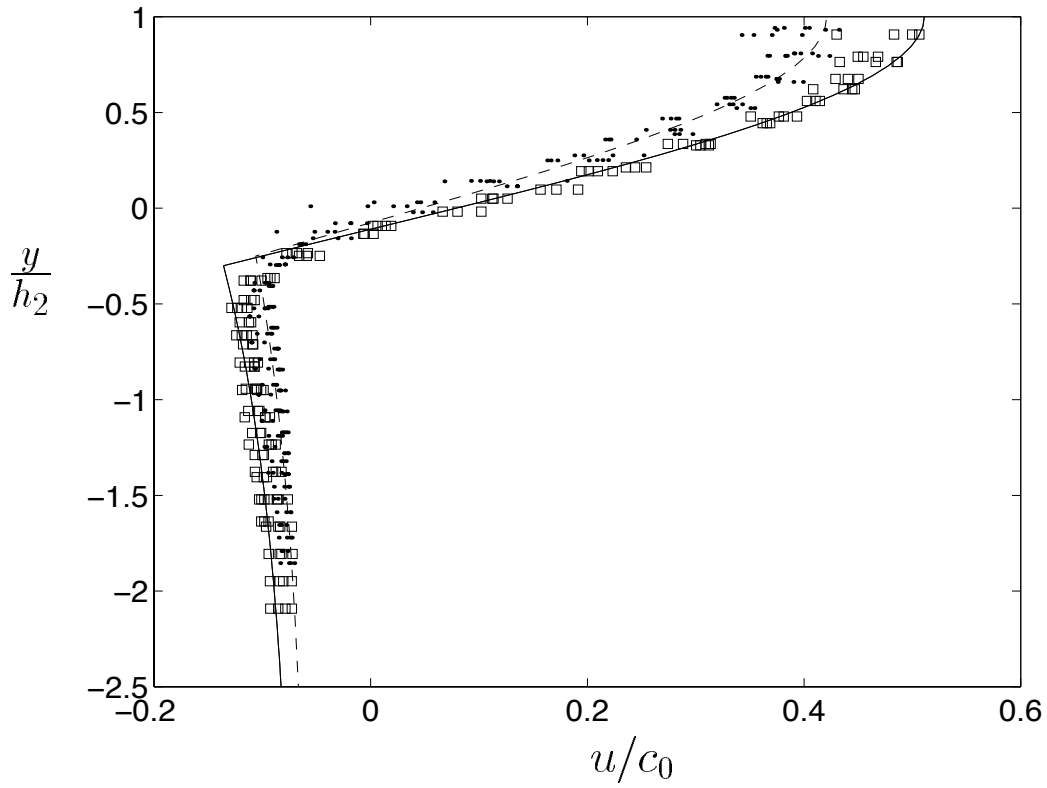
Figure 5: Same as figure 4, but initial volume: 20 dm³. Theory with $a/h_2 = 0.3$ (solid line) and $a/h_2 = 0.25$ (dashed line).
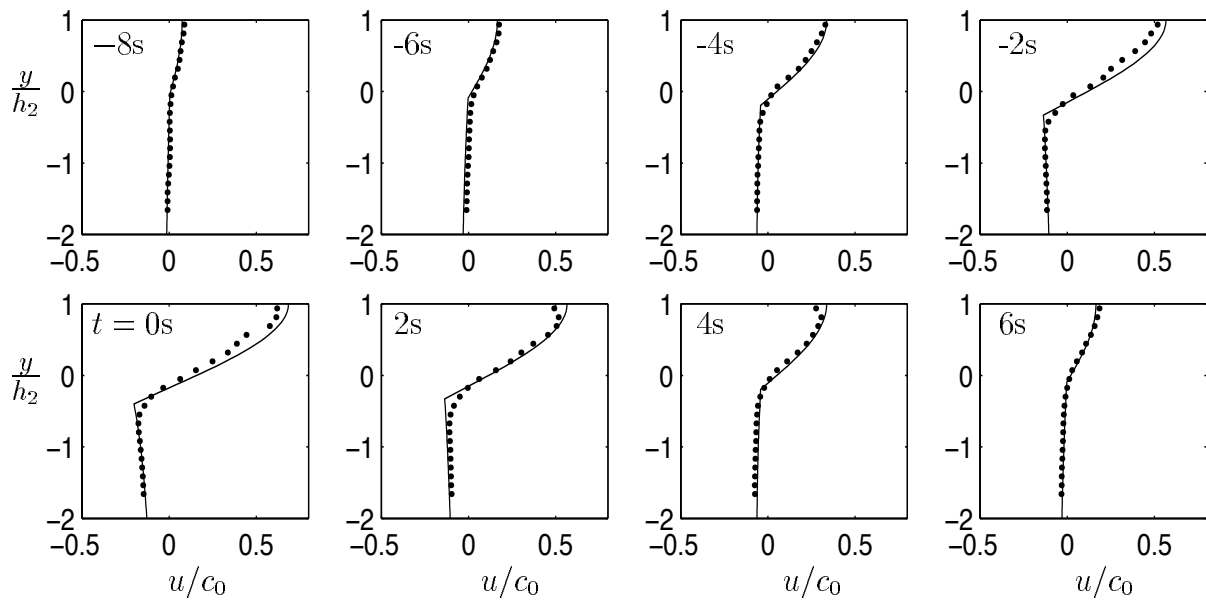
Figure 6: Time series at camera 1 of the horizontal velocity u (abcissa) vs. vertical coordinate y (ordinate). Time increment 2 sec. between each picture. Initial volume: 30 dm³. PTV (dots) and theory with $a/h_2 = 0.4$ (solid line).
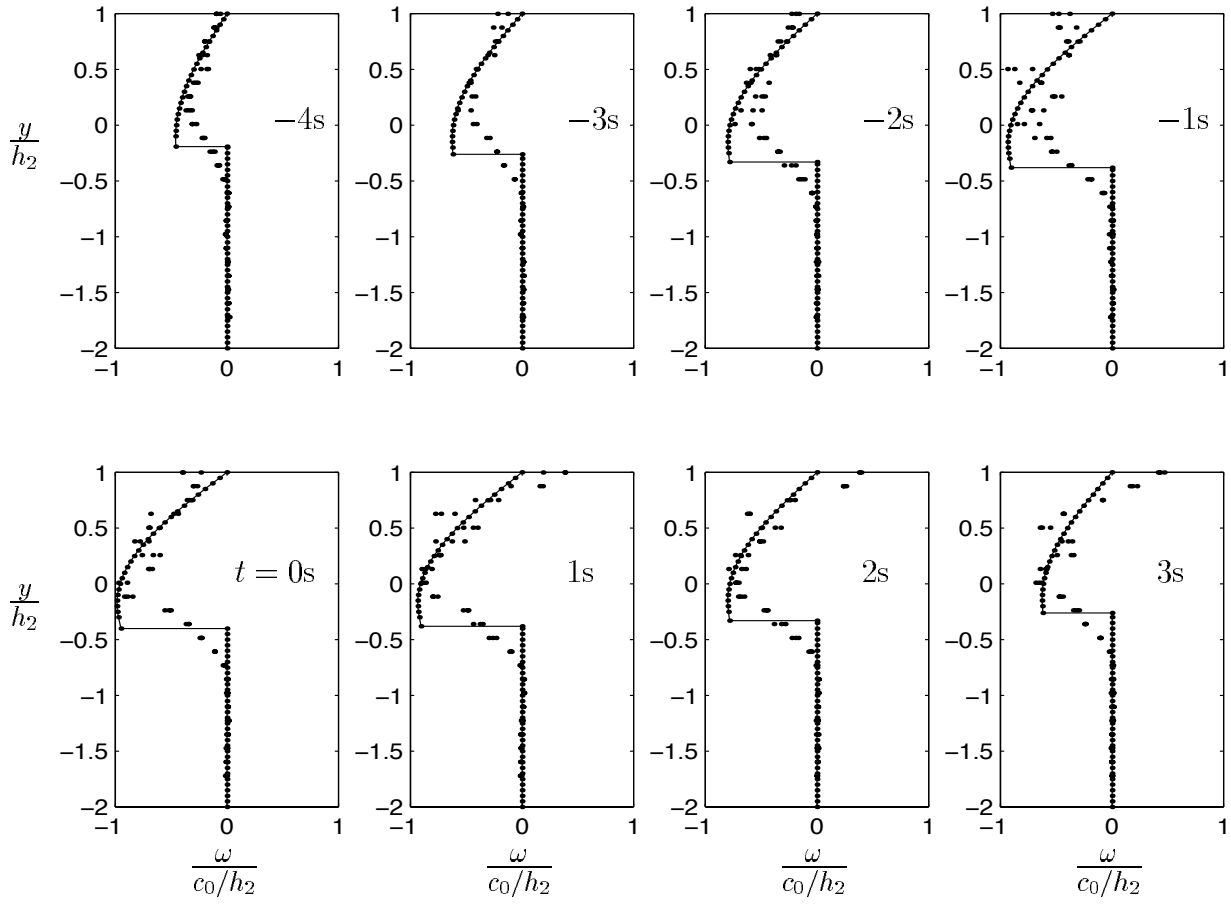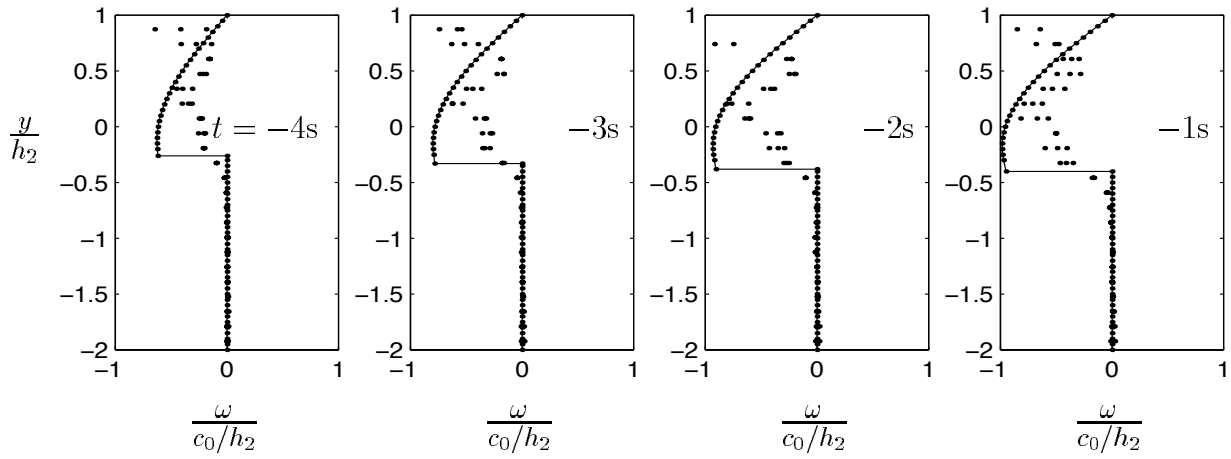
Figure 7: Time series at camera 1 of the vorticity $\omega = \partial u/\partial y - \partial v/\partial x$ (abcissa) vs. vertical coordinate y (ordinate). Time increment 1 sec. between each picture. Initial volume: 30 dm^3. PTV (dots) and theory with $a/h_2 = 0.4$ (solid line with dots).

Figure 8: Same as figure 7, but at camera 2.

6 Waves with moderate amplitude

In the next experiments we generate waves with larger amplitude. Now the induced fluid velocity at the free surface becomes about the linear long wave speed c_0, but significantly less than the propagation speed c of the wave. Examples of the velocity profile at the maximal depression of the wave are displayed in figure 9. The results are obtained from several runs with recordings at all the three camera positions. The theoretical and measured velocity profiles compare rather well. The comparison is particularly good below a region close to the free surface.

It is, however, rather evident that small velocity fluctuations are present in the experiments close to the free surface. These fluctuations may be investigated more closely by examining the vorticity induced by the waves. The vorticity in the experiments is evaluated from the PIV analysis by a least squares operator, i.e. $(df/dx)_i = (2f_{i+2} + f_{i+1} - f_{i-1} - 2f_{i-2})/(10\Delta X)$, Raffel, Willert and Kompenhans (1998, p. 159), while the theoretical vorticity is given by (5). At the first camera we find, apart from some not very pronounced fluctuations of the experimental vorticity, a relatively good correspondence between theory and experiment (figure 10).

At the position of camera 2 we observe a behaviour of the flow which is different from that at camera 1. Now rather pronounced vortices appear in the leading part of the wave, approximately in the middle of the stratified layer. The vortices are visualized in figure 11 by a pronounced negative vorticity in the fore part of the wave for y/h_2 in the interval about $0.5 - 0.7$ and an almost vanishing vorticity for y/h_2 about $0.2 - 0.4$. The formation of the vortices are not described by the theory. We observe the appearance of the vortices in several different runs. It turns out that they appear in the same manner each time, as illustrated in figure 11, where results from two subsequent runs with almost identical characteristics are shown. The vortices continue to develop during the propagation of the wave, as found in the recordings of camera 3 further down in the tank (figure 12). The results in the latter figure is due to a different run, where the density gradient and the speed of the wave are somewhat smaller than for the runs in figures 10–11. The results illustrate that a continuous production of vortices in the leading part of the wave takes place in the experiments. The production of vortices seems to increase with time, according to the development of the vorticity at the different camera positions (figures 10–12).

To visualize the vortices more directly we decompose the velocity field by $\mathbf{v} = \overline{\mathbf{v}} + \mathbf{v}'$. Here $\overline{\mathbf{v}}$ denotes an averaged fluid velocity close to the free surface at the centre of the wave, being approximately equal to $c_0\mathbf{i}$ for the runs in figures 9b and 10–12. The perturbation velocity field $\mathbf{v}'$ contains local vortices in the fore part and in the centre of the waves (figure 13). Similar results (not shown here) are also obtained for smaller waves, with amplitude $a/h_2 \simeq 0.5$ (figure 9a). The vortices are then somewhat less pronounced. We note that separate recordings of the fluid velocities at the free surface from above show that the motion is two dimensional.

The vorticity in the experiments exhibit some oscillations along the vertical coordinate in addition to the pronounced vorticity in the leading part of the wave already described. The oscillations is present both in the upper and in the lower fluid, where in the latter the density is constant. An explanation of these oscillations is uncertain, but we may speculate if they are due to inaccuracies in the recording technique. A high resolution PIV system would perhaps provide better evidence on this point. The oscillations of the vorticity is, on the other hand, much less than the pronounced vorticity caused by the vortices in the fore part of the waves.

The vorticity at the free surface extracted from PIV analysis is almost always rather large and positive (figures 10–12). Truncation effects may, however, distort the velocity

and vorticity estimation close to the boundaries of the pictures. The vorticity obtained from the experiments at the free surface, or in close vicinity of the free surface, may therefore not be accurate.

7   Waves with largest or almost largest amplitude

We have performed several experiments by gradually increasing the initial volume above the levels already described. As already noted, the experiments are calibrated such that only a single solitary wave is generated. This is achieved by appropriately adjusting the position of the gate. An increased initial volume leads to an increased amplitude and propagation speed of the wave, until limiting values are reached (§4). The same is true for the induced fluid velocity which magnitude becomes saturated. The breaking of the waves, taking place in the form of generation of vortices, increases in power when the waves become larger. In this section detailed results for the velocity profiles and the vorticity in two different runs are presented, one for the almost largest wave, and one for the largest. Furthermore, the issues of limiting fluid velocity and broadening of the waves are considered, with results from several runs.

7.1   Velocity profiles

Results for two typical runs are given. The initial volume of the first run is 100 dm^3, while the second is 200 dm^3. The time-history of the profile of the horizontal velocity component $u(y; t)$ is evaluated at the position of camera 3 (figures 14–15). The velocity is scaled by the propagation speed c of the wave. The nondimensional amplitude and propagation speed, determined as described in §4, are $a/h_2 \simeq 1.0$ and $c/c_0 \simeq 1.6$ for the 100 dm^3 wave, and $a/h_2 \simeq 1.2$ and $c/c_0 \simeq 1.7$ for the 200 dm^3 wave.

The measured fluid velocity at the free surface, or close to the free surface, is found to have a maximal value which slightly exceeds the propagation speed of the wave. This is true for both runs. The fluid motion exhibits fluctuations in the region above $y = 0$ which are due to the vortices induced in the leading part of the wave, see figure 18. Below $y = 0$, there are only minor such fluctuations. The velocity profile $u(y; t)$ is symmetric with respect to the centre of the wave when the amplitude is small (§5). The large amplitude waves, however, are not entirely symmetric. The deviation from symmetry is obviously caused by the non-symmetric presence of the large number of small vortices in the large waves.

While the two different runs have several features in common, there are also some important differences to be noted. The most visible difference is the time period between arrival and disappearance of the wave at a position of the tank. This is longer for the larger wave than for the smaller, which means that the wave with the larger initial volume is broader than the other. Secondly, the larger wave has a longer and somewhat thicker region in the upper part of the wave where the horizontal velocity is approximately equal to the propagation speed c. More presicely, the fluid velocity in this region is $\mathbf{v} = c\mathbf{i} + \mathbf{v}'$, where $\mathbf{v}'$ contains small fluctuating velocities due to a number of vortices generated by the flow.

7.2   Vorticity

The velocity fluctuations may be further examined by evaluating the vorticity component $\omega = \partial u/\partial y - \partial v/\partial x$ (figures 16–17). This vorticity component exhibits rather strong oscillations in the upper region of the wave where the velocity field has fluctuations. The

vorticity oscillates about a nonzero mean. The oscillations of the vorticity illustrate the intensity and scale of the vortices which are generated in the leading part and above the centre of the wave, see also figure 18.

While the motion is two-dimensional for waves with small and moderate amplitude, three-dimensional effects take place for the largest waves. This is illustrated in figure 19 where the wave tank is seen from above. In this figure, recordings of the horizontal velocity field $u'\mathbf{i} + w\mathbf{k} = (u - c)\mathbf{i} + w\mathbf{k}$ right below the free surface, in the leading part of the wave, are presented. ($w\mathbf{k}$ denotes the horizontal velocity component across the wave tank.) Pronounced velocity fluctuations across the wave tank are found in the recordings. The vorticity component $\partial w/\partial x - \partial u/\partial z$, where z is the coordinate across the wave tank, is also shown in the figure. This vorticity component exhibits oscillations which are of the same order of magnitude as for $\omega = \partial u/\partial y - \partial v/\partial x$. We have not been able to measure the vorticity component $\partial v/\partial z - \partial w/\partial y$. This requires equipment for three-dimensional PIV, which we do not have available.

7.3   Broadening

Figures 14–15 show that the waves broaden when the volume of the wave exceeds a certain value. The broadening effect is further illustrated in figure 20, where the time history of the horizontal fluid velocity close to the free surface is displayed as function of time for several initial volumes. Since the experimental velocities contain fluctuations close to the free surface, and since the velocity estimates from the PIV analysis at the free surface are somewhat uncertain, we display the time history of the velocity averaged over a small vertical distance close to the free surface, i.e.

$$\overline{u}(t) = \int_{0.5h_2}^{0.9h_2} u(y, t)\, dy \,/\, (0.4h_2)\,. \tag{41}$$

We find in these experiments that the waves begin to broaden for an initial volume of approximately 70 dm³. The results further show that $\overline{u}_{max}$, defined by the maximal value of $\overline{u}(t)$ in each run, may become slightly larger than the propagation speed c of the wave. This is due to the perturbation velocity field $\mathbf{v}'$ which is superposed on the velocity $c\mathbf{i}$. More presicely, we obtain that $\overline{u}_{max}/c \simeq 1.03$.

We may also evaluate the wavelength as defined by

$$\lambda = \frac{1}{\overline{u}_{max}} \int_{-\infty}^{\infty} \overline{u}\, dx = \frac{1}{\overline{u}_{max}} \int_{-\infty}^{\infty} \overline{u}(t)\, c\, dt\,. \tag{42}$$

The experiments show that the wave length decays with increasing wave amplitude (and $\overline{u}_{max}/c$), for small and moderate waves. The waves broaden, however, when $\overline{u}_{max}/c$ exceeds the value of 0.8, approximately (figure 21). The corresponding nondimensional wave amplitude is then about $a/h_2 = 0.8$. The wavelength estimated from both experiments and theory is shown in the figure, with good agreement for $\overline{u}_{max}/c < 0.8$ (and $a/h_2 < 0.8$). The boadening effect seen in the experiments is not present in the theory, however.

8 Concluding remarks

We have investigated the characteristic properties of solitary waves of depression propagating in a stratified fluid. The fluid has a shallow upper layer with linear stratification and a deep lower layer with constant density. The investigation combines experiments and theory. The experiments are facilitated by the recent developments of particle tracking velocimetry (PTV) and particle image velocimetry (PIV). These techniques able recordings of rather detailed behaviour of the induced velocities of the waves. We also determine the propagation speed from the velocimetry techniques.

Particular focus is paid to the role of the breaking of the waves. Incipient breaking takes place by formation of vortices in the leading part of the waves. When incipient breaking occurs, the fluid velocity close to the free surface is comparable to the linear long wave speed, and the wave amplitude is about half of the depth of the shallow layer. The breaking increases in strength with increasing amplitude and serves to limit the amplitude of the wave, the propagation speed and the magnitude of the induced fluid velocities. The maximal amplitude in these experiments becomes 1.25 times the depth of the upper layer, while the maximal propagation speed is 1.8 times the linear long wave speed, approximately. A typical feature of the large waves is a region in the upper part of the wave with pronounced local variations of the velocity field and the vorticity. For the largest waves, the horizontal fluid velocity in this region is approximately equal to the propagation speed c of the wave. More precisely, the fluid velocity is $\mathbf{v} \sim c\mathbf{i} + \mathbf{v}'$, where $\mathbf{v}'$ describes the velocity field due to a number of vortices. In the observations $|\mathbf{v}'|$ is significantly less than c.

When the fluid velocity becomes approximately equal to the propagation speed of the wave, the fluid particles may be transported over long distances by the waves. Knowledge of mass transport due to internal waves may contribute to the general understanding of transportation of water masses in the ocean. Moreover, it may contribute to the understanding of specific geological and biological issues like how e.g. sediments or larvae are transported in the ocean. Since solitary waves may occur in a similar way in a layered atmosphere as in a layered ocean, we also expect that a similar mass transport may take place in the atmosphere.

We find that broadening takes place when the volume of the waves exceeds a certain value. This effect is clearly documented from the experiments. The broadening is obviously caused by the wave breaking which serves to limit the magnitude of the induced fluid velocity, the amplitude and the speed of the wave. More specifically, broadening is found to take place when the maximal fluid velocity exceeds 0.8 times the speed of the wave, approximately. The wave amplitude is then about 0.8 times the depth of the shallow layer. The broadening effect found here is entirely different from the one which takes place in a two-fluid system with constant densities in each of the layers. In the latter case, the limited amplitude and wave speed, and thereby the broadening of the waves, are determined by a finite total depth of the fluid (Amick & Turner, 1986; Turner and Vanden-Broeck, 1988; Grue et al., 1997; 1999).

With the purpose of interpreting and providing a relief of the experimental results, we develop a theoretical and numerical model of the waves. This is a two-layer model, where the upper layer has constant Brunt-Väisälä frequency and the lower layer has zero Brunt-Väisälä frequency. Wave solutions are obtained by means of integral equations. Comparisons between the experimental and theoretical velocity fields exhibit relatively good agreement for small and moderate waves. The intrinsic breaking of the waves is not, however, modelled by the theory. This becomes most evident by comparing the vorticity in the experiments and the theory. Since the wave breaking determines the limiting amplitude, the limiting wave speed and the broadening of the wave, none of these results

can be determined by the theoretical model applied here (nor in the models by e.g. Tung et al., 1982; Turkington et al., 1991; Brown & Christie, 1998).

The theory may, on the other hand, be used to broaden the picture of the experimental results. We have here so far performed a detailed experimental and theoretical investigation for only one ratio $h_1/h_2 = 4.13$ between the depths of the layers. Now we may apply the theoretical model to predict the velocity fields for other depth ratios. The intention is to investigate if the velocity field induced by the waves, for other values of h_1/h_2, is similar to that for $h_1/h_2 = 4.13$. The results in figures 22–23 for $h_1/h_2 = 2, 3, 4.13, 10, 100$ show in fact that the velocities and shapes of the waves are rather similar when h_1/h_2 is larger than about 3. The same is true for c/c_0, see table 1 below. Since the breaking of the waves are caused by the intrinsic dynamics of the velocity field induced by the propagating wave, the results here lead us to expect that breaking occurs in a same manner as described in sections 6-7, beginning at a/h_2 about 0.5, for all depths h_1/h_2 larger than about 3. This also means that the wave amplitude and propagation speed have limiting values being close to those we have found here, and that the waves broaden in a similar way for all depth ratios h_1/h_2 larger than about 3.

h_1/h_2	2	3	4.13	10	100
$c/c_0(a/h_2 = 0.65)$	1.33	1.36	1.38	1.39	1.38
$c/c_0(a/h_2 = 0.8)$	1.40	1.44	1.46	1.48	1.47

Table 1: Theoretical propagation velocity c/c_0 as function of layer thickness ratio h_1/h_2 for waves with amplitudes $a/h_2 = 0.65$ and $a/h_2 = 0.8$.

(a)

(b)

(c)

u/c_0
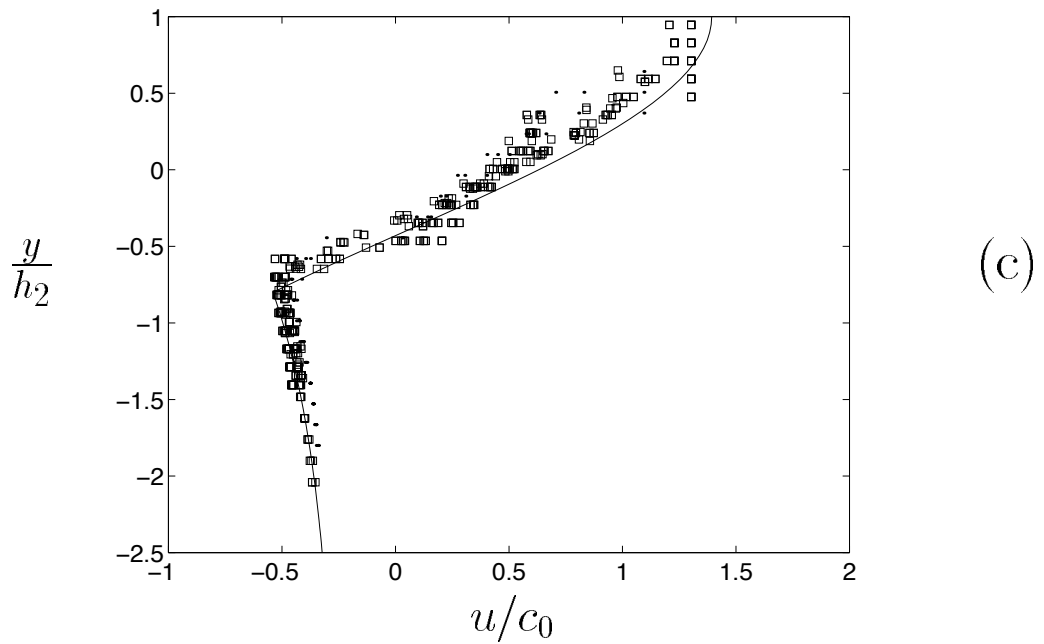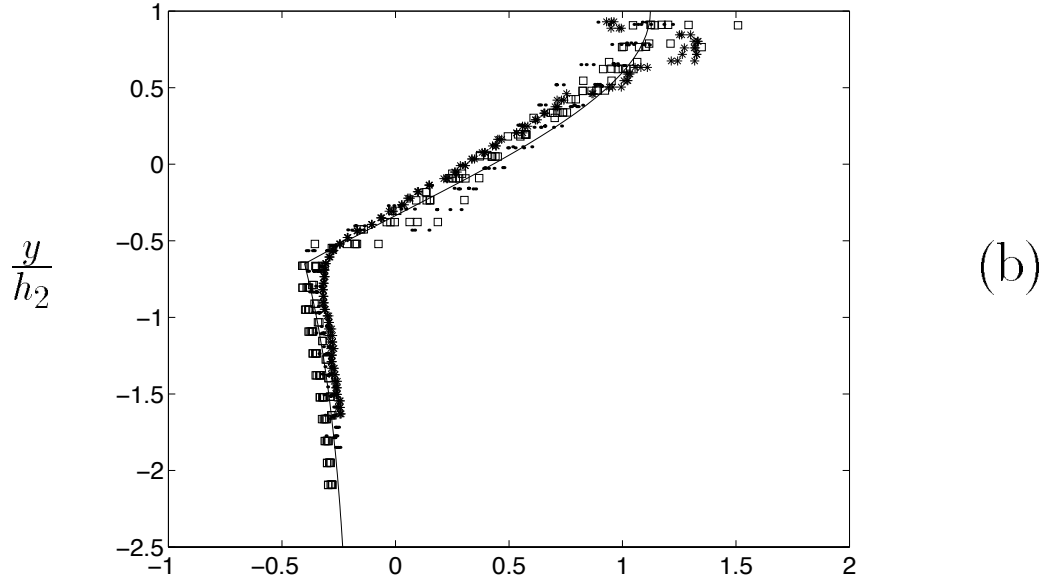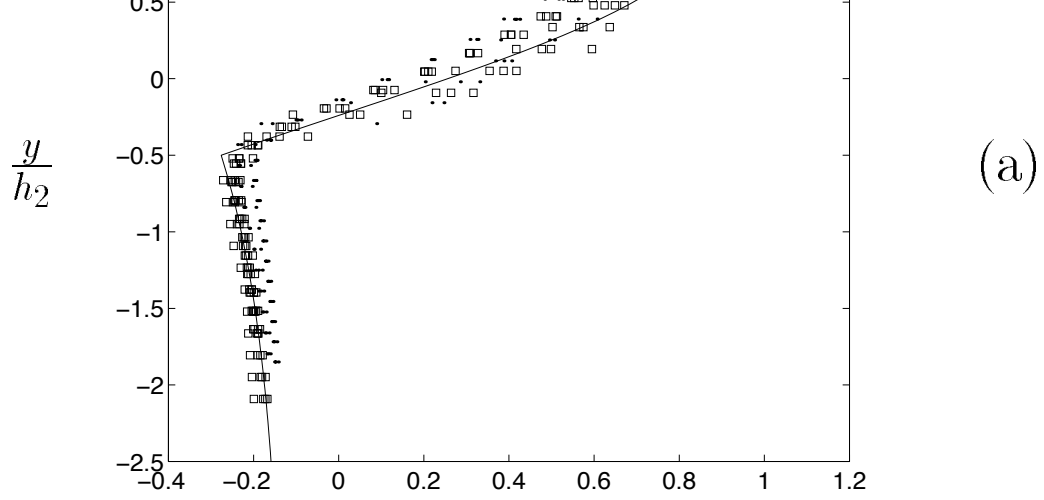
Figure 9: Same as figure 4, but (a) PTV, initial volume 40 dm^3, theory with $a/h_2 = 0.5$ (solid line), (b) PTV and PIV, initial volume 50 dm^3, theory with $a/h_2 = 0.65$ (solid line), (c) PTV and PIV, initial volume 65 dm^3 and theory with $a/h_2 = 0.8$ (solid line). (note the differences in scale.)
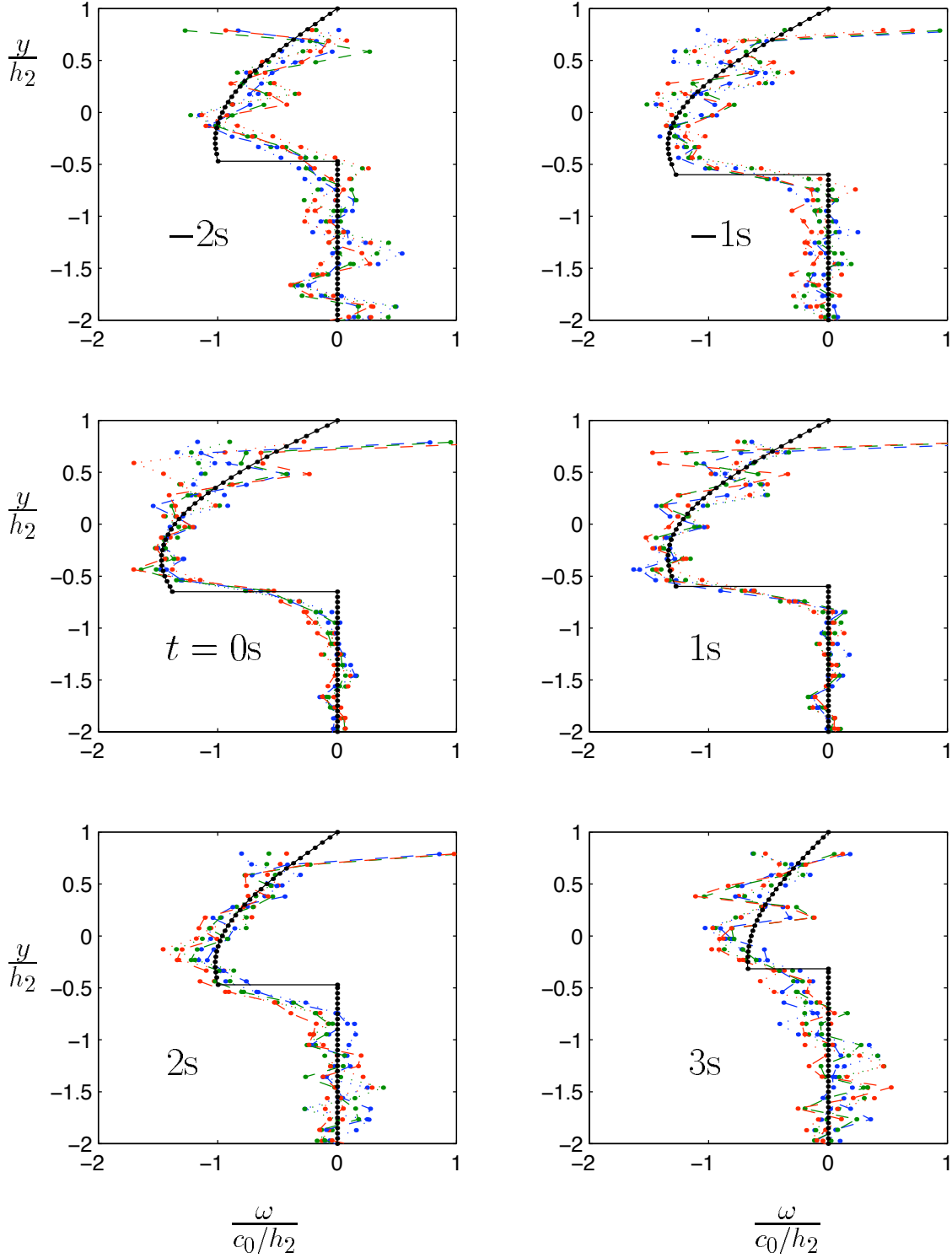
Figure 10: Time series at camera 1 of the vorticity $\omega = \partial u/\partial y - \partial v/\partial x$ (abcissa) vs. vertical coordinate y (ordinate). $\Del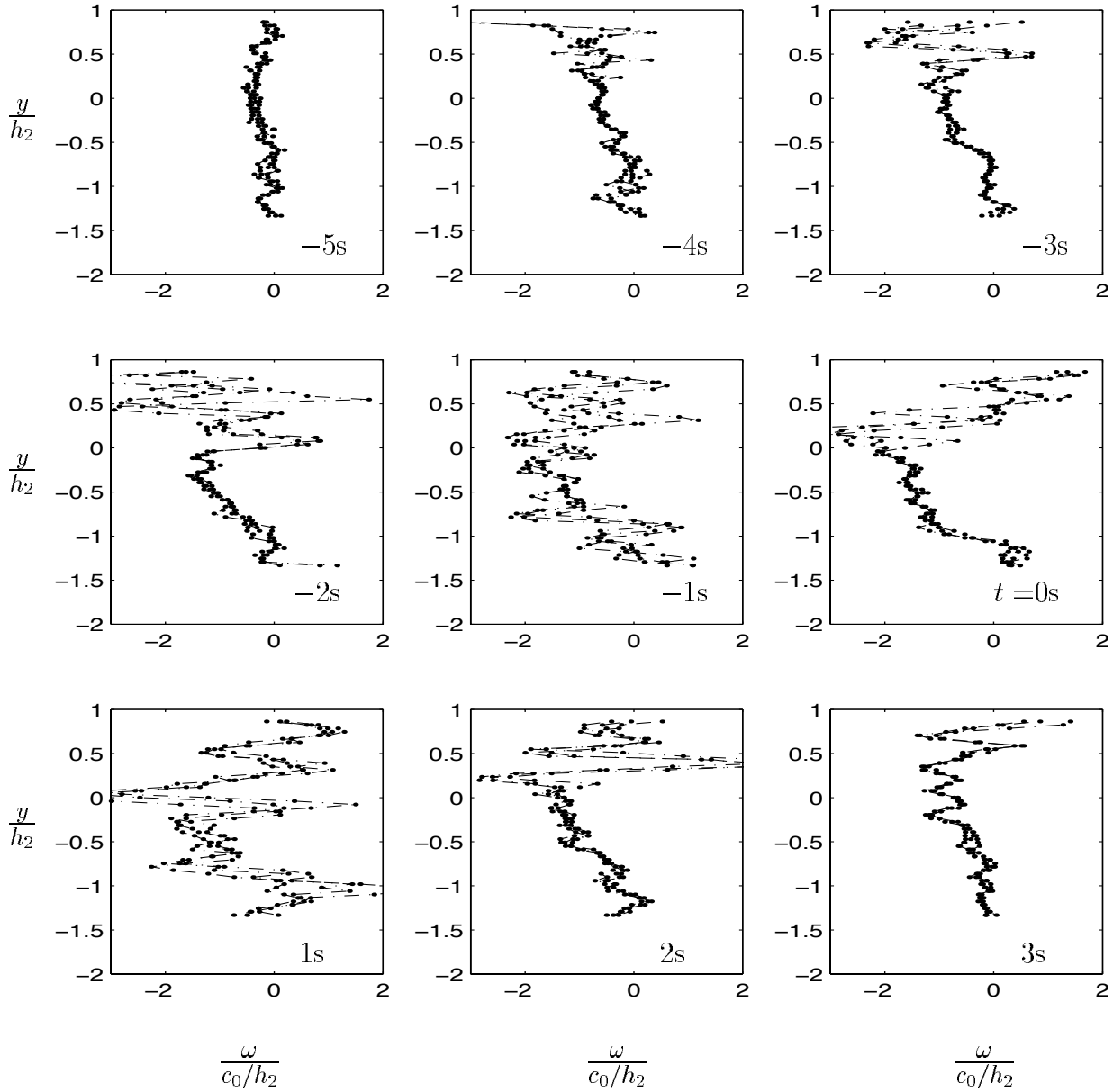ta t = 1$ sec. between each picture. Initial volume: 50 dm³. PIV. Two different runs. Run 1: $\rho_0 = 1.0226$gcm⁻³, $\rho_1 = 0.9989$gcm⁻³, $c_0 = 11.38$cms⁻¹ (dash-dotted line). Run 2: $\rho_0 = 1.0225$gcm⁻³, $\rho_1 = 0.9991$gcm⁻³, $c_0 = 11.36$cms⁻¹) (dotted line). Theory (solid line). $t = 0$s means middle of the wave.
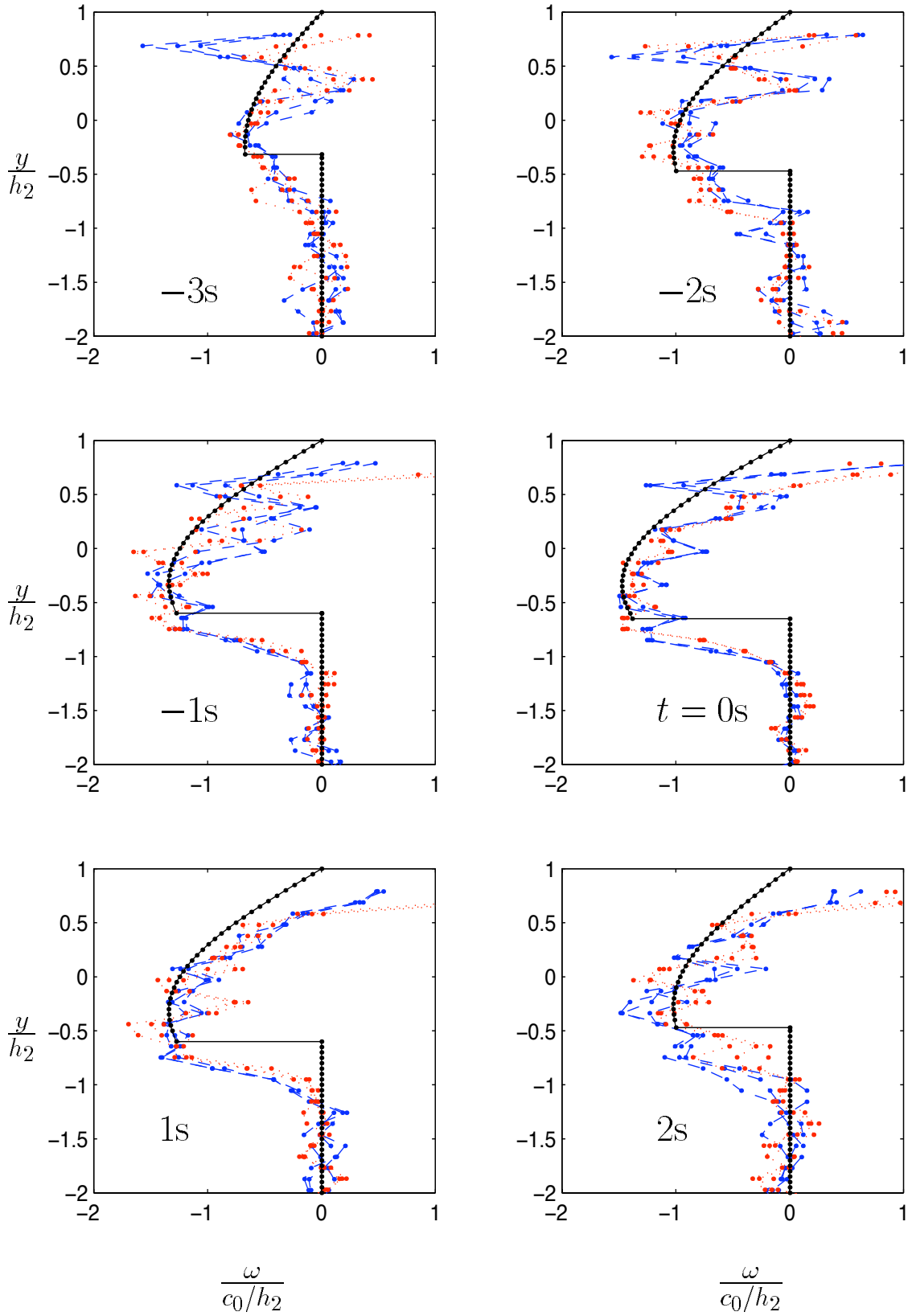
Figure 11: Same as figure 10, but camera 2.
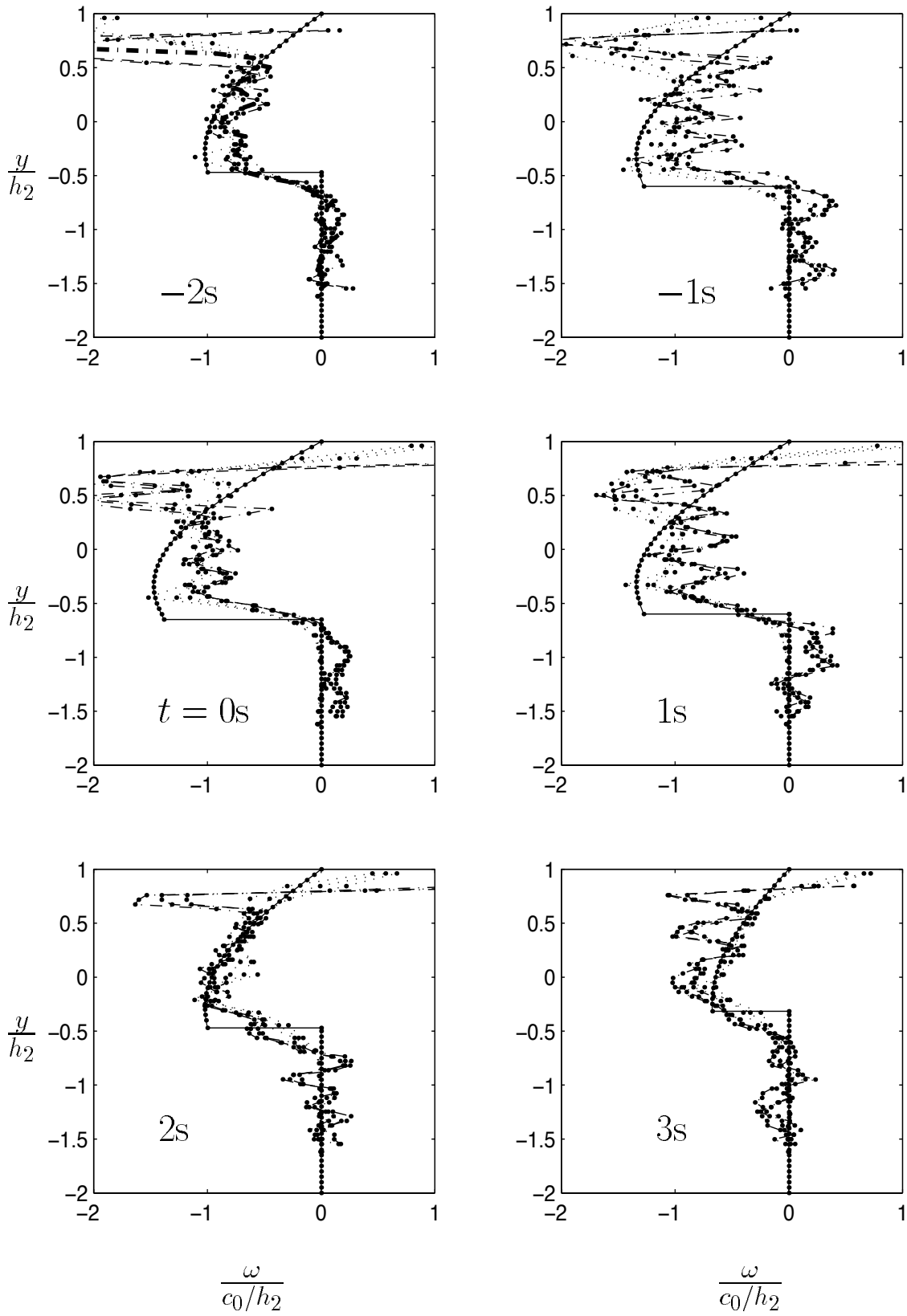
Figure 12: Same as figures 10 and 11, but camera 3. Different run than in figures 10–11. $\rho_0 = 1.0225 \mathrm{gcm}^{-3}$ $\rho_1 = 1.0040 \mathrm{gcm}^{-3}$ $c_0 = 9.01 \mathrm{cms}^{-1}$. PIV (dots with solid line), PTV (dots with dotted line), theory (solid line).

$t = -2\mathrm{s}$

$t = -1\mathrm{s}$

$t = 0\mathrm{s}$
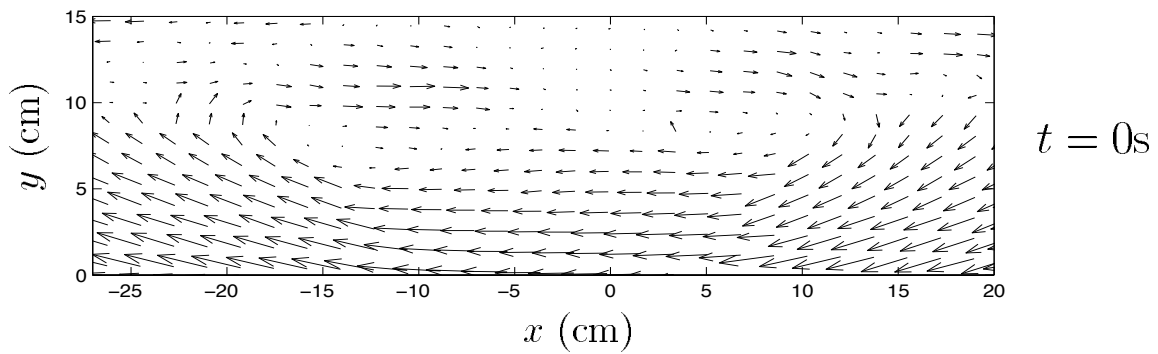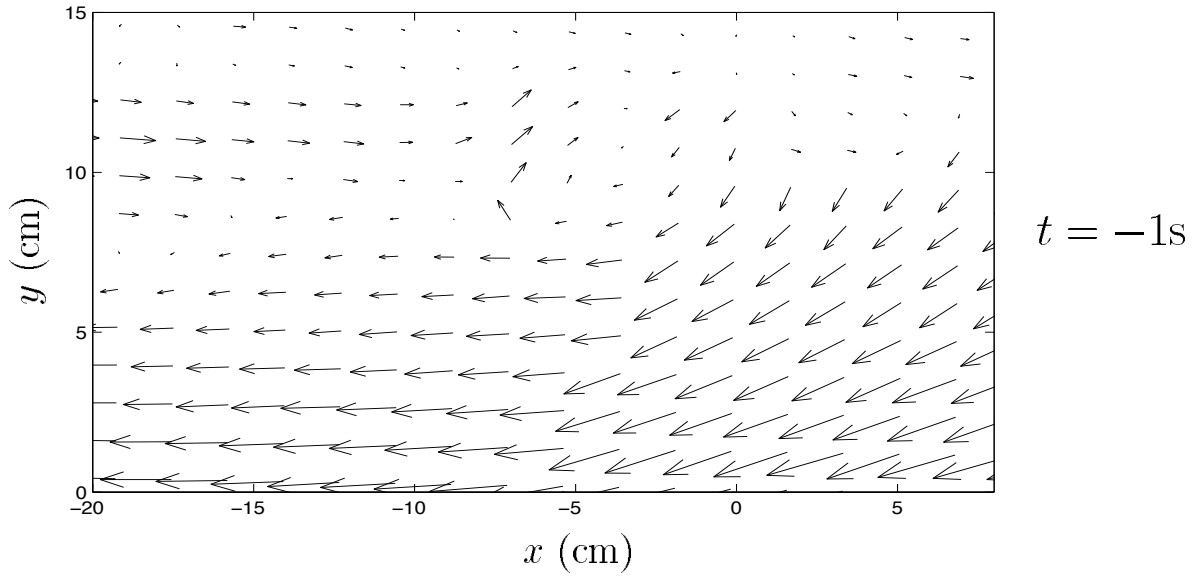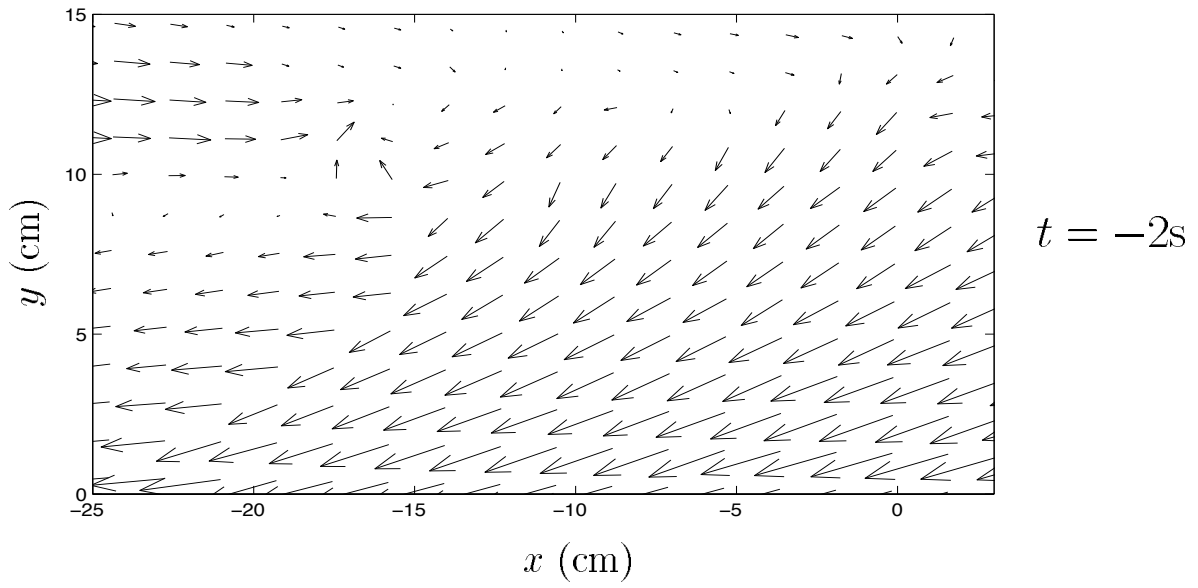
Figure 13: Velocity field $\mathbf{v} - c_0\mathbf{i}$. Initial volume 50 dm^3. Camera 3. Close up of the region $0cm < y < 15cm$ below the free surface (where the latter is at $y = 15cm$). (For reference: the depth of the upper layer at rest is $15cm$.) $t = 0$s means middle of the wave.
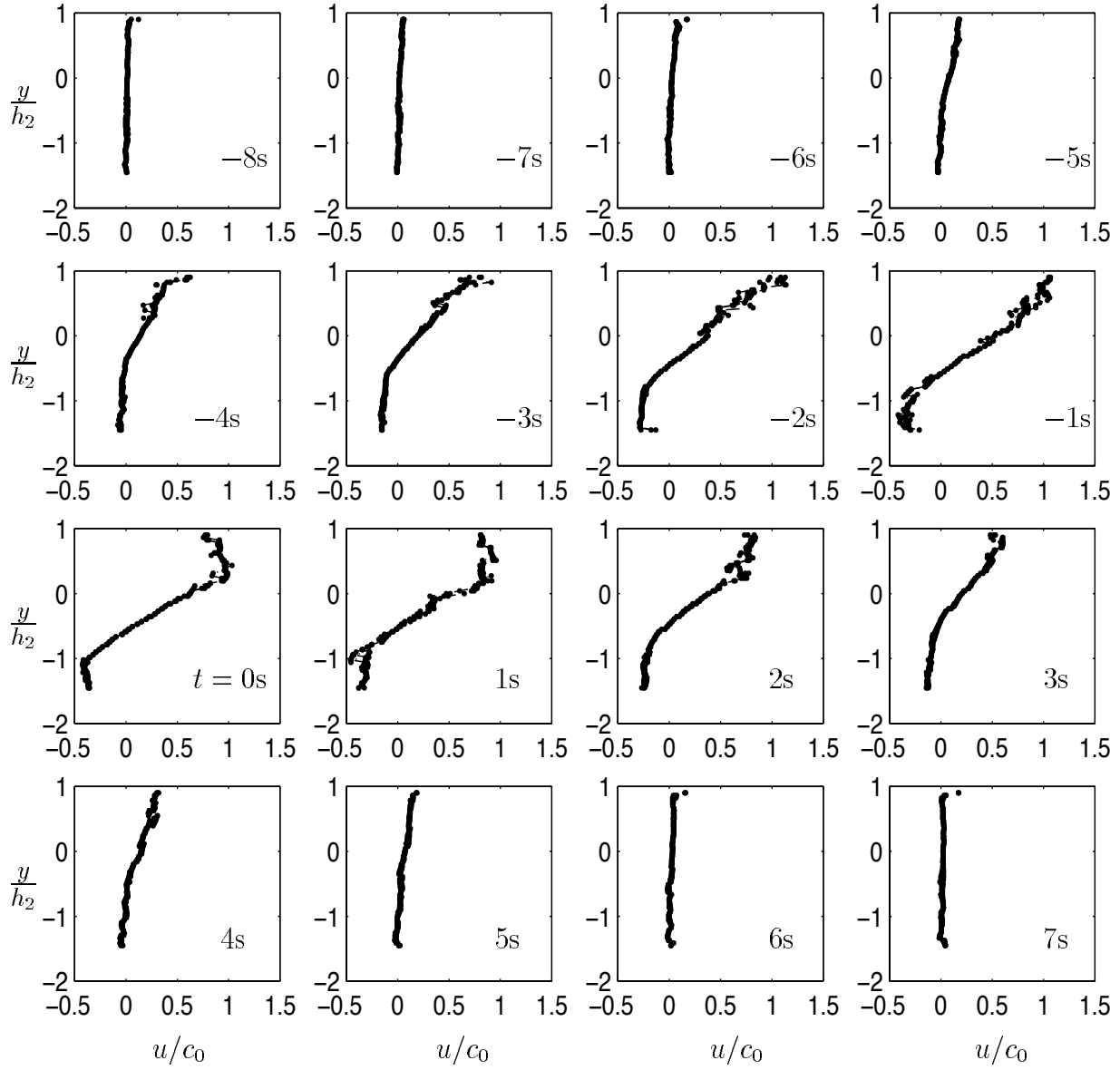
Figure 14: Time series of the horizontal velocity u (abcissa) vs. vertical coordinate y (ordinate). PIV at camera 3. Time increment 1 sec. between each picture. Initial volume 100 dm^3.
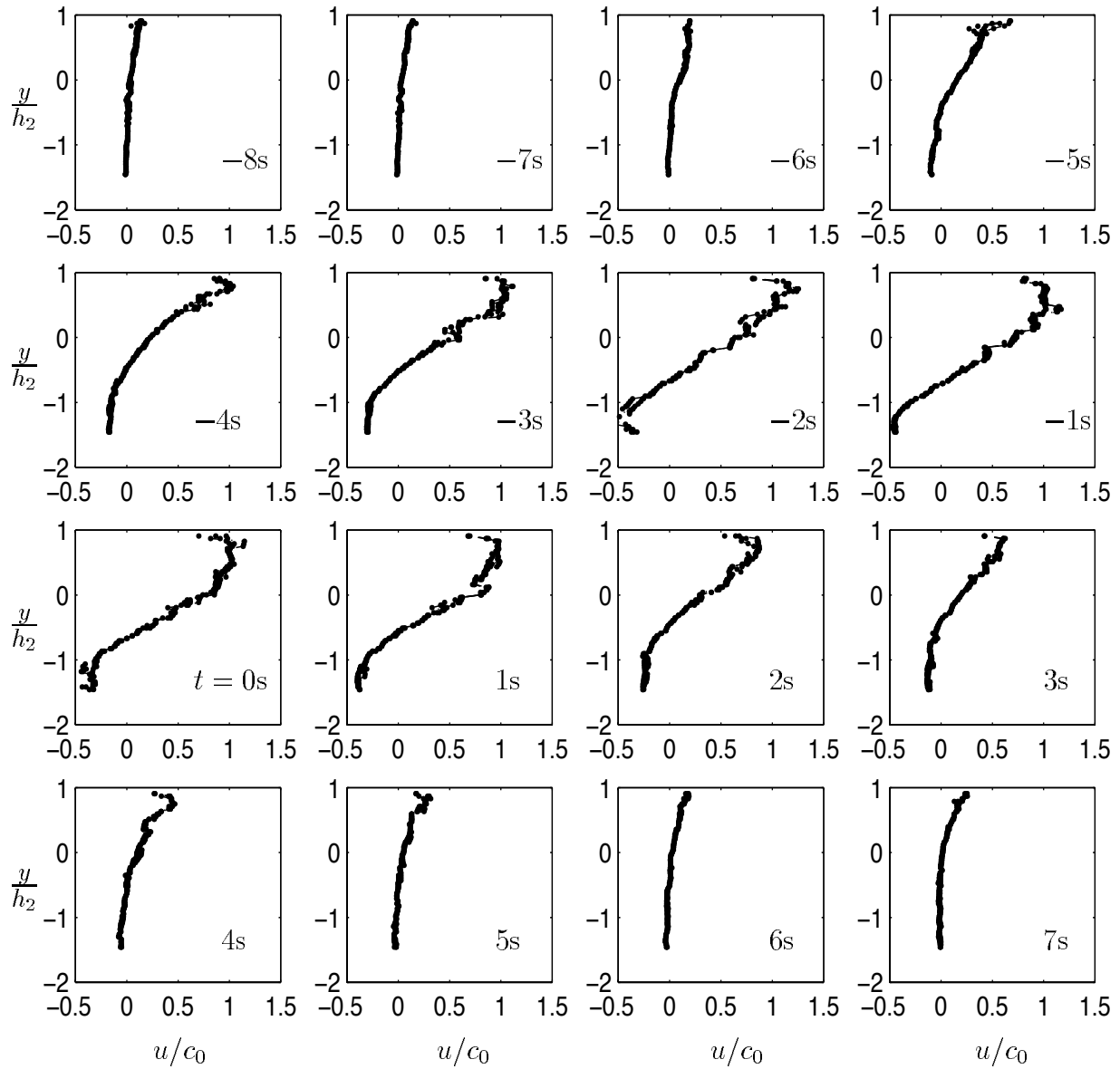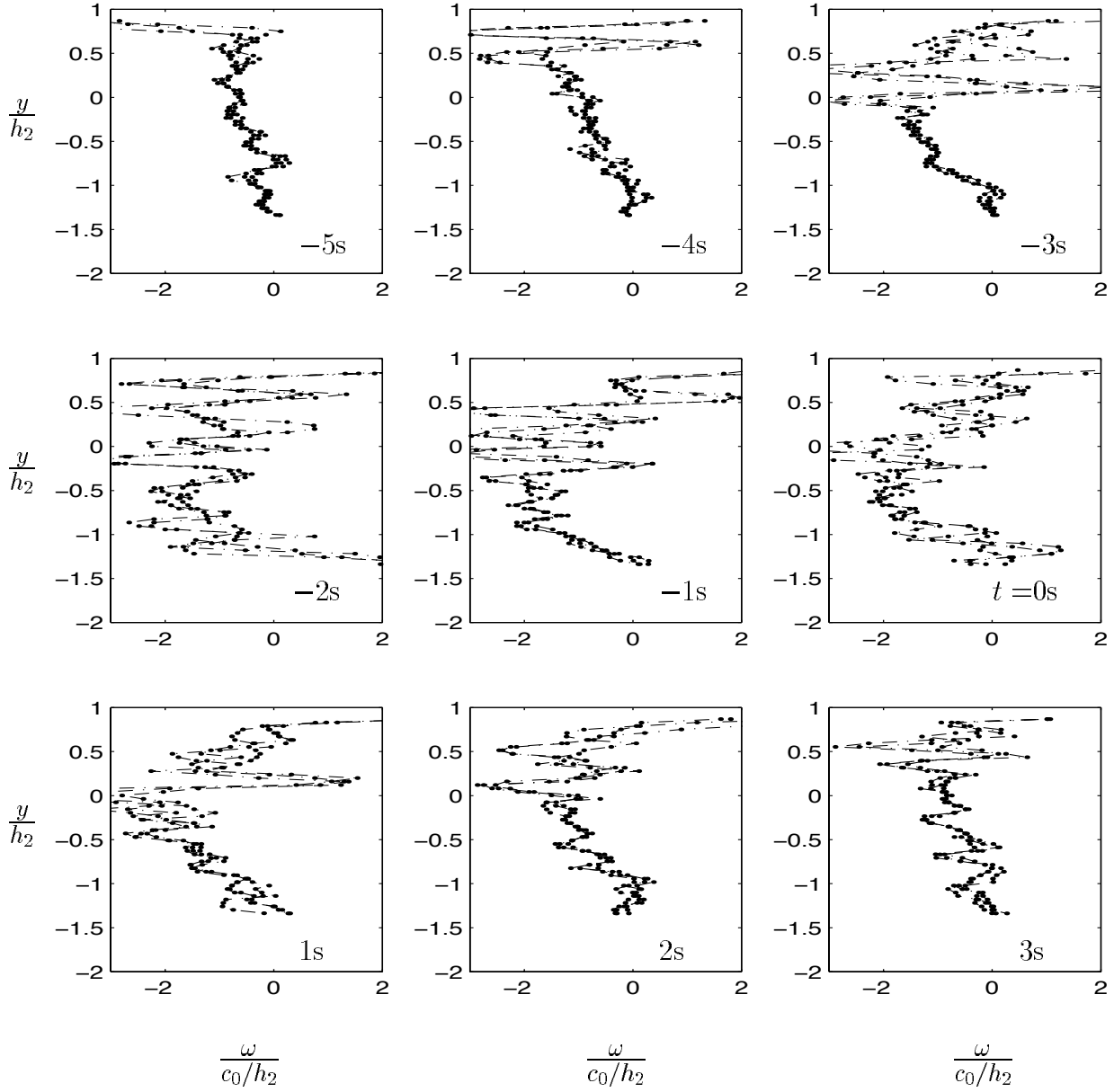
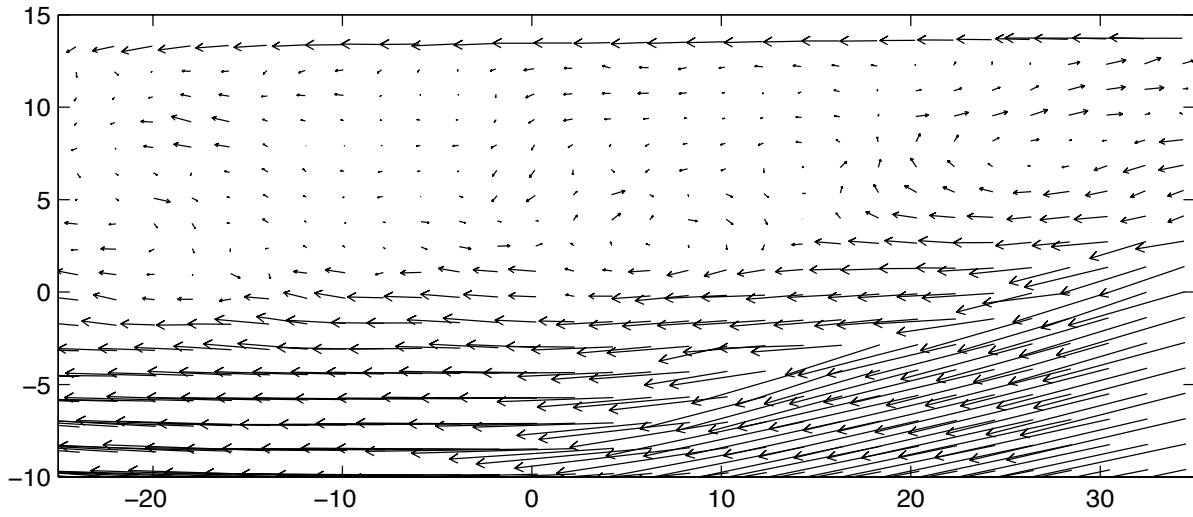Figure 15: Same as figure 14, but initial volume 200 dm^3.

Figure 16: Time series of the vorticity $\omega = \partial u/\partial y - \partial v/\partial x$ (abcissa) vs. vertical coordinate y (ordinate). PIV at camera 3. Time increment 1 sec. between each picture. Initial volume 100 dm^3.

Figure 17: Same as figure 16, but initial volmue 200 dm^3.

Figure 18: Velocity field $\mathbf{v} - c\mathbf{i}$. Close up of the region $-10cm < y < 15cm$ below the free surface (at $y = 15cm$). (For reference: the depth of the upper layer at rest is $15cm$.) Camera 3. Initial volume 200 dm^3.
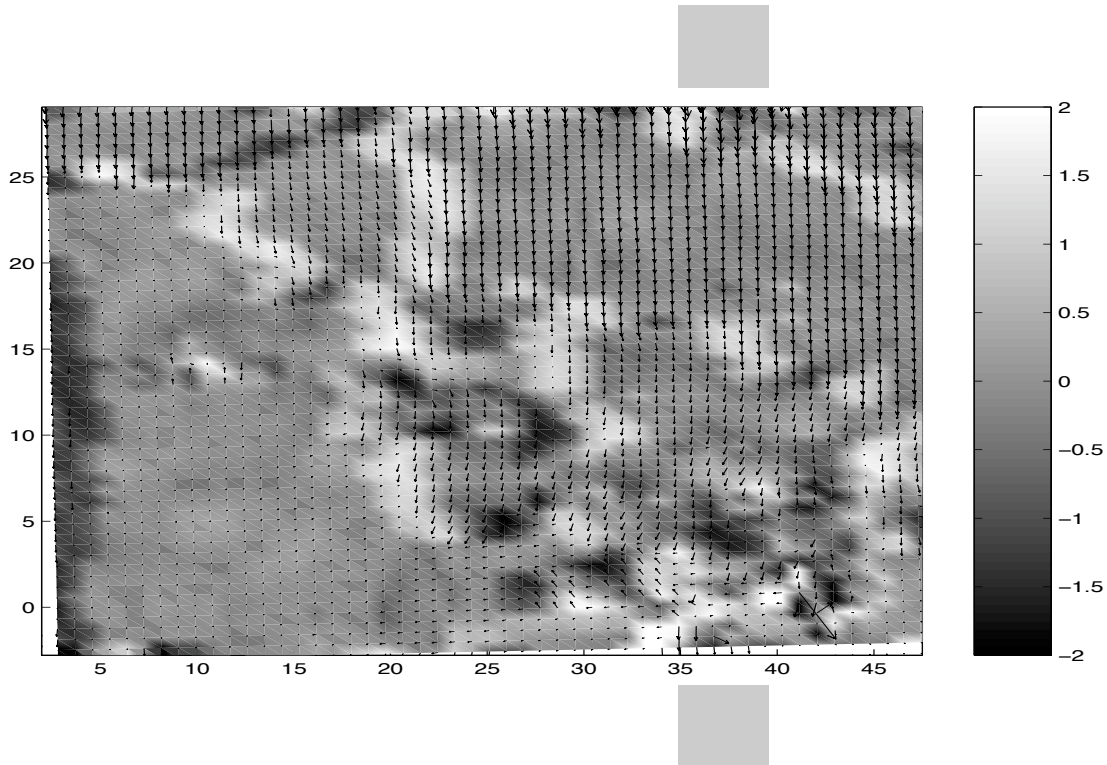

Figure 19: Horizontal velocity field $u\mathbf{i} + w\mathbf{k} - c\mathbf{i}$ at the free surface. Wave tank viewed from above. Vorticity component $(\partial w/\partial x - \partial u/\partial z)/(c_0/h_2)$ in grey scale. Initial volume 200 dm^3. Recording section 50 cm $\times$ 35 cm. The position of the vertical light sheet in the recordings, except this one, is between the positions of the grey boxes.
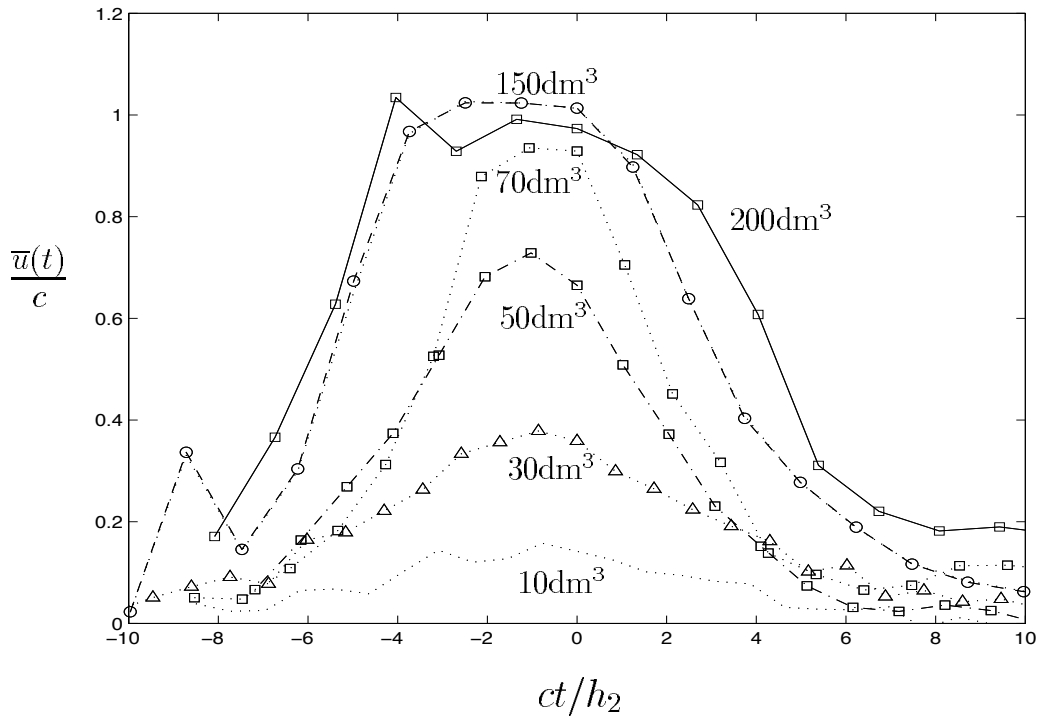
Figure 20: Broadening of the waves. $\overline{u}(t)/c$ vertical line vs. ct horizontal line. Initial volume: 10 dm^3, 30 dm^3, 50 dm^3, 70 dm^3, 150 dm^3, 200 dm^3.
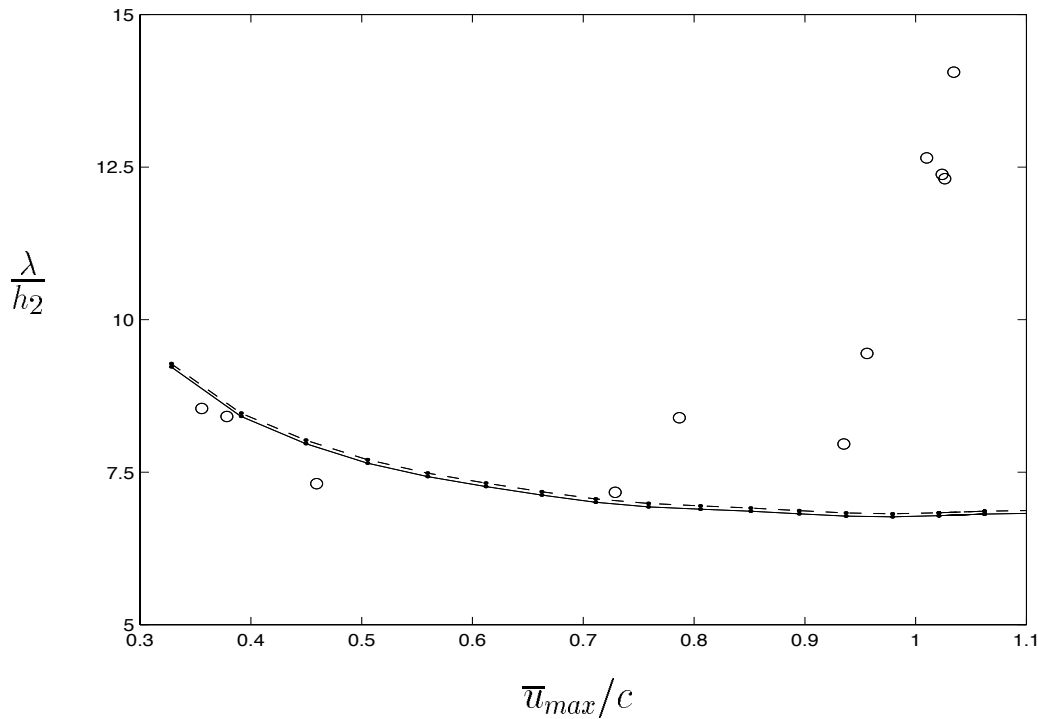

Figure 21: Wavelength λ as defined in eq. (42) vs. $\overline{u}_{max}/c$. Experiments (small circles) and theory (solid line). Also theoretical $\lambda = \int_{-\infty}^{\infty} u(y = h_2, t)\, c\, dt / u(y = h_2)_{max}$ (dashed line).
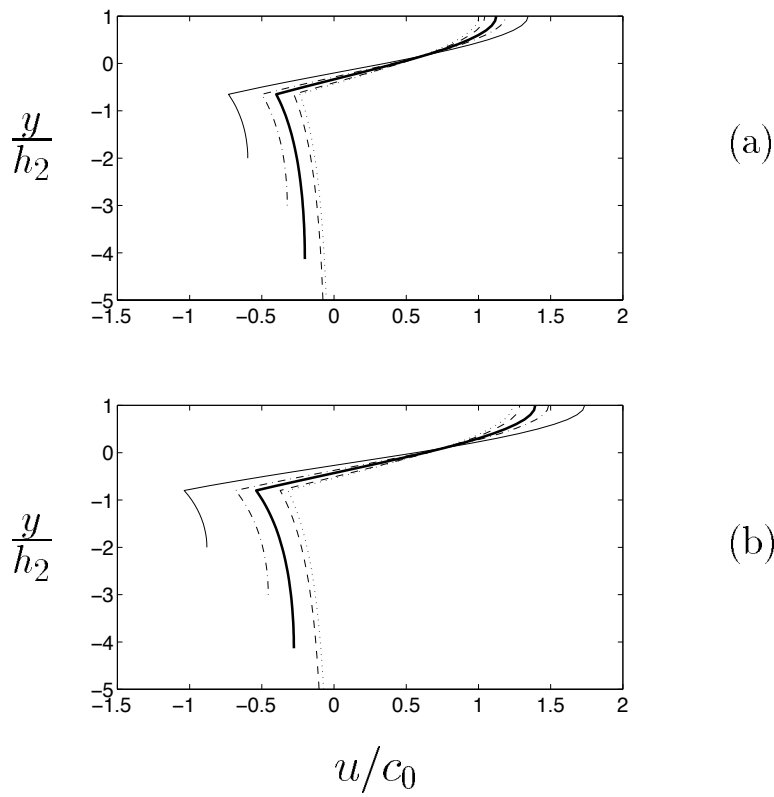
31

Figure 22: Theoretical velocity profiles at maximal wave depression. Depth-ratio h_1/h_2: 2 (thin solid line), 3 (dash-dot line), 4.1333 (thick solid line), 10 (dashed line) and 100 (dotted line). (a) $a/h_2 = 0.65$. (b) $a/h_2 = 0.80$.
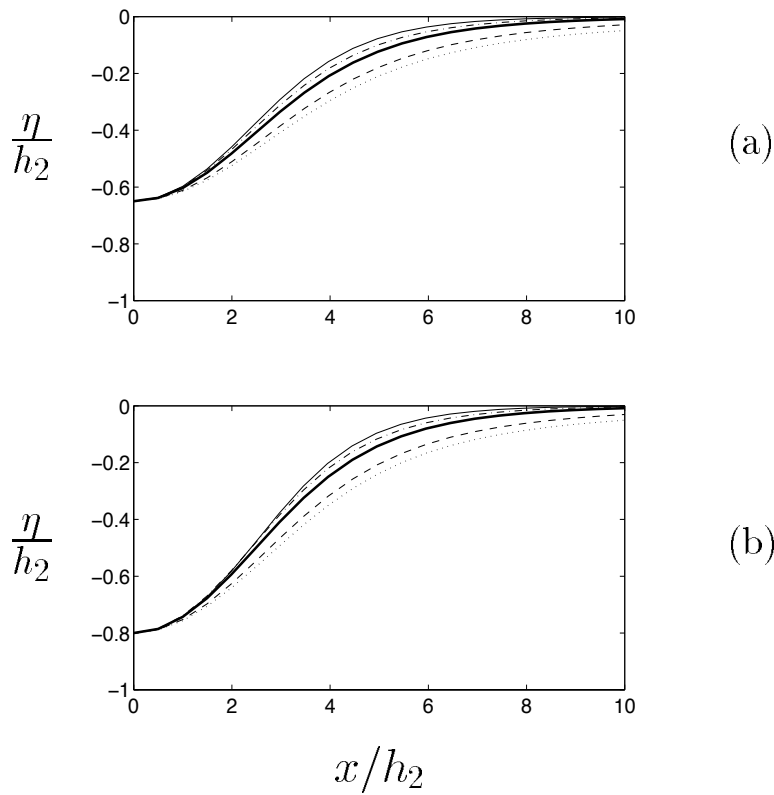

Figure 23: Same as figure 22, but depression of the line η separating the layers.

References

[1] AMICK, C. J. AND TURNER, R. E. L. 1986 A global theory of internal solitary waves in two-fluid systems. *Trans. Am. Math. Soc.*, **298**, 431.

[2] APEL, J. R., HOLBROOK, J. R., LIU, A. K. AND TSAI, J. 1985 The Sulu Sea internal soliton experiment. *J. Phys. Oceanography.* **15**, 1625.

[3] BROWN, D. J AND CHRISTIE, D. R. 1998 Fully nonlinear solitary waves in continuously stratified incompressible Boussinesq fluids. *Phys. Fluids*, **10**, 2569.

[4] DALZIEL, S. B. 1992 Decay of rotating turbulence: some particle tracking experiments. *Applied Scientific Research*, **49**, 217..

[5] DAVIS, R. E. AND ACRIVOS, A. 1967 Solitary internal waves in deep water. *J. Fluid Mech.*, **29**, 593.

[6] DERZHO, O. G. AND GRIMSHAW, R. 1997 Solitary waves with a vortex core in a shallow layer of stratified fluid. *Phys. Fluids*, **9**, 3378.

[7] DOLD, J. W. AND PEREGRINE, D. H. 1985 An efficient boundary-integral equation method for steep unsteady water waves. *Numerical Methods for Fluid Dynamics*, **2**, edited by K. W. Morton and M. J. Baines, Clarenden Press, Oxford., pp. 671-670.

[8] DUDA, T. 1998 Editor, IOS/WHOI/ONR Internal Solitary Wave Workshop, Victoria B.C., Canada.
<http://www.whoi.edu/science/AOPE/people/tduda/isww>.

[9] FARMER, D. M. AND SMITH, J. D. 1980 Tidal interaction of stratified flow with a sill in Knight Inlet. *Deep-Sea Res.*, **27A**, 239.

[10] GRUE, J., FRIIS, A., PALM, E. AND RUSÅS, P.-O. 1997 A method for computing unsteady fully nonlinear interfacial waves. *J. Fluid Mech.*, **351**, 223.

[11] GRUE, J., JENSEN, A., RUSÅS, P.-O. AND SVEEN, J. K. 1999 Properties of large amplitude internal waves. *J. Fluid Mech.*, **380**, 257.

[12] LONG, R. R. 1958 Tractable models of steady-state stratified flow with shear. *Q. J. R. Meteorol. Soc.*, **84**, 159.

[13] MAXWORTHY, T. 1980 On the formation of nonlinear internal waves from the gravitational collapse of mixed regions in two and three dimensions. *J. Fluid Mech.*, **96**, 47

[14] RAFFEL, M., WILLERT, C. AND KOMPENHANS, J. 1998 Particle Image Velocimetry. Springer.

[15] STAMP, A.P. AND JACKA, M. 1995 Deep-water internal solitary waves. *J. Fluid Mech.*, **305**, 347.

[16] SVEEN, J. K. (1998) An introduction to MatPIV v.1.1. Documentation and code:
<http://www.math.uio.no/~jks>.

[17] TUNG, K. K, CHAN, T. F. & KUBOTA, T. 1982 Large amplitude waves of permanent form. *Stud. Appl. Math.*, **16**, 1.

[18] TURKINGTON, B., EYDELAND, A. & WANG, S. 1991 A computational method for solitary internal waves in a continuously stratified fluid. *Stud. Appl. Math.*, **85**, 93.

[19] TURNER, R. E. L. AND VANDEN-BROECK, J.-M. 1988 Broadening of interfacial solitary waves. *Phys. Fluids*, **31**, 372.

[20] WESTERWEEL, J., DABIRI, D. AND GHARIB, M. 1997 The effect of a discrete window offset on the accuracy of cross-correlation analysis of digital PIV recordings. *Experiments in Fluids*, **23**, 20.

[21] WILLERT, C. E. AND GHARIB, M. 1991 Digital particle image velocimetry. *Experiments in Fluids*, **10**, 181.

[22] YIH, C.-S. 1960 Exact solutions for steady two-dimensional flow of a stratified fluid. *J. Fluid Mech.*, **9**, 161.